mTORC1 Controls Phase Separation and the Biophysical Properties of the Cytoplasm by Tuning Crowding

Morgan Delarue, G Brittingham, S. Pfeffer, I Surovtsev, S Pinglay, K. Kennedy, M Schaffer, J. Gutierrez, D Sang, G Poterewicz, et al.

To cite this version:

Morgan Delarue, G Brittingham, S. Pfeffer, I Surovtsev, S Pinglay, et al.. mTORC1 Controls Phase Separation and the Biophysical Properties of the Cytoplasm by Tuning Crowding. Cell, Elsevier, 2018. hal-02273800

HAL Id: hal-02273800
https://hal.archives-ouvertes.fr/hal-02273800

Submitted on 29 Aug 2019

Title: mTORC1 controls phase separation and the biophysical properties of the cytoplasm by tuning crowding

Authors: M. Delarue[1,9], G.P. Brittingham[1,9], S. Pfeffer[8,9], I.V. Surovtsev[2,5,6], S. Pinglay[1], K.J. Kennedy[3], M. Schaffer[8], J.I. Gutierrez[3], D. Sang[1], G. Poterewicz[1], J.K. Chung[4], J. Plitzko[8], J.T. Groves[4,5], C. Jacobs-Wagner[2,5,6,7], B.D. Engel[8*] and L.J. Holt[1*]

Affiliations:

[1] Institute for Systems Genetics, New York University Langone Health, New York, NY 10016, USA

[2] Department of Molecular, Cellular, and Developmental Biology, Yale University, New Haven, CT 06511

[3] Department of Molecular and Cell Biology University of California, Berkeley, Berkeley CA 95720, USA

[4] Department of Chemistry University of California, Berkeley, Berkeley CA 95720, USA

[5] Howard Hughes Medical Institute, Chevy Chase, MD 20815, USA

[6] Microbial Sciences Institute, Yale West Campus, West Haven, CT 06516, USA

[7] Department of Microbial Pathogenesis, Yale School of Medicine, New Haven, CT 06511, USA

[8] Department of Molecular Structural Biology, Max Planck Institute of Biochemistry, 82152 Martinsried, Germany

[9] These authors contributed equally

* Correspondence to: liam.holt@nyumc.edu , engelben@biochem.mpg.de

Summary (Abstract): *(less than 150 words)*

Macromolecular crowding has a profound impact on reaction rates and the physical properties of the cell interior, but the mechanisms that regulate crowding are poorly understood. We developed Genetically Encoded Multimeric nanoparticles (GEMs) to dissect these mechanisms. GEMs are homomultimeric scaffolds fused to a fluorescent protein. GEMs self-assemble into bright, stable fluorescent particles of defined size and shape. By combining tracking of GEMs with genetic and pharmacological approaches, we discovered that the mTORC1 pathway can modulate the effective diffusion coefficient of macromolecules ≥20 nm in diameter more than 2-fold by tuning ribosome concentration, without any discernable effect on the motion of molecules ≤5 nm. These mTORC1-dependent changes in crowding and rheology affect phase separation both *in vitro* and *in vivo*. Together, these results establish a role for mTORC1 in controlling both the biophysical properties of the cytoplasm and the phase separation of biopolymers.

Introduction

Molecular crowding is crucial for the efficient function of biological systems (Zhou et al., 2008). If *Xenopus* egg extracts are diluted by more than a few percent, fundamental biological processes such as mitosis and DNA replication fail (Lohka and Maller, 1985). High concentrations of crowding agents entropically favor molecular association events, thereby accelerating molecular reactions (Rivas et al., 2001; Zhou et al., 2008). However, excessive crowding can also dramatically decrease molecular motion, just as the loss of a lane on a freeway can transform smooth traffic flow to instant gridlock (Miermont et al., 2013; Trappe et al., 2001).This kind of jamming depends strongly on particle size: molecules with sizes equivalent to or larger than the dominant crowding agent will be more affected than small particles that can move through the gaps left at the intersections of jammed crowding particles. Thus, changes in molecular crowding can have profound effects on cell physiology and may affect some pathways disproportionately, depending on the sizes of the molecules involved.

A key example where regulation of macromolecular crowding is paramount is phase separation. Proteins that have a stronger propensity to self-associate than to interact with the solute can undergo a phase transition, where a large number of interacting proteins coalesce into a condensed liquid phase that is separate from the surrounding bulk liquid solute (Banani et al., 2016; Brangwynne et al., 2009). These biological condensates are increasingly observed in diverse fields including cell division (Woodruff et al., 2017; 2015), development (Brangwynne et al., 2009), cancer (Grabocka and Bar-Sagi, 2016; Kaganovich et al., 2008), neurodegenerative disease (Kwon et al., 2014), T-cell activation (Alberti and Hyman, 2016; Su et al., 2016), and even photosynthesis

(Freeman Rosenzweig et al., 2017). Macromolecular crowding tunes phase separation *in vitro* (Banani et al., 2016). However, the physiological mechanisms that control crowding within the cell and the effects of crowding on cellular processes remain obscure.

One method to study macromolecular crowding and other cellular biophysical properties is to observe the motion of nanoscale tracer particles as they move within the cell. This approach, known as passive microrheology, can be used to infer the viscosity, elasticity, structure, and dynamics of the surrounding material from the characteristic motion of these tracer particles (Mourão et al., 2014; Wirtz, 2009). Various groups have studied the motion of non-biological nanoparticles in cells (Daniels et al., 2006; Luby-Phelps et al., 1986), but these techniques are labor intensive and typically perturb the cell. For example, microinjection disrupts the cell membrane and cortex, and is not feasible in organisms with a cell wall, such as budding yeast. An alternative approach is to track the motion of endogenous structures, such as mRNA molecules tagged with specific loops and loop-binding proteins that can be tagged with fluorescent proteins (Shav-Tal et al., 2004). However, if the motion of an endogenous molecule is affected by a perturbation, it is difficult to know if these changes in motion are due to impacts on the biophysical properties of the cell, or rather caused by direct regulation of the tracer particle. Evolutionarily orthogonal biological tracers have been used to address this issue, notably the µNS particle from mammalian rheovirus (Joyner et al., 2016; Parry et al., 2014). These types of tracer particles are less likely to undergo specific regulated interactions with the cell, but a major limitation of the µNS system is that these condensates do not have a predefined size, and thus require additional calibration steps to convert fluorescence measurements into particle size (Joyner et al., 2016; Parry et al., 2014). Furthermore, the size of µNS probes (> 50 nm) is larger than most multimeric protein complexes found inside cells.

In order to address these issues, we developed ***G***enetically ***E***ncoded ***M***ultimeric (GEM) nanoparticles (henceforth GEMs), which are bright tracer particles of a defined shape and size. GEMs can serve as a standard microrheological tool across a broad range of organisms; in this study, we used GEMs in *S. cerevisiae* and human cell lines. By using GEMs from a different kingdom than the organism of study, we make it far less likely that the particles will be affected by specific interactions. With this technology in hand, we screened for mechanisms that regulate the biophysical properties of cells. We found that mTORC1 controls ribosome abundance through a combination of cell volume control, ribosome biogenesis and autophagy. *In situ* cryo-electron tomography (cryo-ET) of the native cellular environment (Asano et al., 2016) revealed that inhibition of mTORC1 nearly halves the cytosolic ribosome concentration. As ribosomes account for ~20% of the total cytosolic volume, modulation of their concentration has a dramatic effect on the biophysical properties of the cell. This modulation is significant: Inhibition of mTORC1 can double the effective diffusion coefficient of particles that are 20 nm in diameter or greater. We derived a theoretical model based on the phenomenological Doolittle equation that relates the diffusion of a tracer particle to the fraction of crowding, and were able to predict changes in the diffusion coefficient as a function of ribosome concentration in both budding yeast (*S. cerevisiae*) and human cells (HEK293). Finally, we found that changes in macromolecular crowding downstream of mTORC1 tune phase separation in both yeast and human cells, providing a direct link between *in vivo* crowding regulation and phase separation.

Results

GEMs can be made from both 15 nm and 35 nm icosahedral protein cages

We developed GEMs to study the rheological properties of the eukaryotic cytoplasm. We began with natural homomultimeric scaffolds that self-assemble into icosahedral geometries and fused these scaffolds to fluorescent proteins (GFP) to create fluorescent GEMs.

In this study, we employed scaffolding domains based on the encapsulin protein from the hyperthermophilic archaeon *Pyrococcus furiosus* (Akita et al., 2007) and the lumazine synthase enzyme complex from the hyperthermophilic bacterium *Aquifex aeolicus* (Zhang et al., 2001) (figure 1A-C). When expressed within cells, these GEMs self-assembled into bright, stable particles (figure 2A-B).

Using *in situ* cryo-ET to image the native cellular environment (Asano et al., 2016), we determined that the *Pyrococcus furiosus* encapuslin GEM has a diameter of 41 nm, a little larger than the 35 nm diameter reported from crystallography data (Akita et al., 2007) (figure 1C). This larger diameter is likely due to the additional GFP molecules decorating the encapsulin particle. Thus, we termed these particles **40nm-GEMs**.

Using negative stain electron microscopy, we measured a diameter of 15 nm for the *A. aeolicus* lumazine synthase GEM (figures 1C and S1A), in good agreement with crystallography data (Zhang et al., 2001) (figure 1C). However, the GFP density was not visible in the low-resolution negative stain images (see also figure S1B, where *Pyrococcus furiosus* encapuslin GEMs are measured at 37 nm). Thus, accounting for the likely extra diameter due to decoration with GFP molecules, we termed these particles **20nm-GEMs**.

The 20nm-GEMs and 40nm-GEMs are in the size range of multi-subunit assemblies such as ribosomes, proteasomes and chromatin remodeling complexes (figure 1D), allowing us to investigate the mesoscale microrheological environment experienced by these complexes. Thus, these biologically-orthogonal nanoparticles probe the biophysical properties of the cell at a length-scale that was previously inaccessible.

GEMs allow rapid characterization of the rheological properties of the cytosol in yeast and human cells

We expressed 40nm-GEMs in the budding yeast *S. cerevisiae* and an adenovirus transformed Human Embryonic Kidney cell line (HEK293, (Russell et al., 1977)) (figure 2A-B, supplemental movies 1-2). 40nm-GEMs are bright enough to allow single particle tracking at 10 ms frame rates (figure 2C, see methods). The duration of tracking is limited to the amount of time a particle remains in focus, as the particles move too fast to allow for direct z-tracking. The median trace length was 35 frames, corresponding to 350 ms of imaging (figure S1C). We compared thousands of individual traces to extract the effective coefficient of diffusion, D_{eff}, at short timescales (100 ms). GEM motilities differ between the two biological systems: 40nm-GEMs have a median effective diffusion coefficient of ~0.3 $\mu m^2\ s^{-1}$ in yeast and ~0.5 $\mu m^2\ s^{-1}$ in mammalian cells (figure 2D-E). These estimates are in good agreement with expectations from the literature (Luby-Phelps et al., 1986), further supporting the use of GEMs as microrheological standards. Using time and ensemble-averaging, we inspected the mean-squared displacement (MSD) curves at longer timescales and found that 40nm-GEMs were subdiffusive (inset figure 2D-E, S2A) with an anomalous exponent of ~0.8 in yeast and ~0.9 in HEK293 cells. This subdiffusive motion could be due to local caging within a crowded environment and/or interactions between the tracer particle and the environment (Wang et al., 2012). However, the anomalous exponent did not change significantly in most of our perturbation experiments (figure S2A), so we focused on the apparent diffusion coefficient as our main metric to report on cytosolic rheology.

mTORC1 affects the biophysical properties of the cytosol

In initial experiments in yeast, we observed that cell culture conditions changed the apparent diffusion coefficients of 40nm-GEMs. When yeast cultures approached saturation, the effective diffusion of GEMs increased (figure S2B). By specifically depleting nitrogen, glucose and amino acids, the main components of synthetic complete growth medium, we found that both nitrogen and glucose starvation caused a slight decrease in the apparent diffusion of 40nm-GEMs, but this decrease was subtle compared to previous reports with larger particles (Joyner et al., 2016; Munder et al., 2016a) (figure S2D). In contrast, we found that an increase in effective diffusion occurred in response to amino acid depletion (figure S2C).

The mechanistic target of rapamycin complex (mTORC1) is the major amino acid sensor in *eukaryotes* (Hara et al., 1998). Therefore, we hypothesized that mTORC1 signaling might cause the observed changes in cytoplasmic rheology in response to perturbations in amino acid levels. mTORC1 can be inhibited by addition of rapamycin, which forms an inhibitory complex with the protein FKBP 12 (encoded by *FPR1* in *S. cerevisiae*) (Heitman et al., 1991). Consistent with our hypothesis, 40nm-GEMs displayed increased mobility upon inhibition of mTORC1 with rapamycin in both *S. cerevisiae* and HEK293 cells (figure 2D-E, supplemental movies 1-2). This increase in effective diffusion reached full effect after 2 and 3 hours of rapamycin treatment in yeast and HEK293 cells, respectively (figure S2E). Changes in the distribution of diffusion coefficients were highly significant ($p < 1 \times 10^{-41}$ for yeast and $p < 1 \times 10^{-40}$ for HEK293; Kolmogorov-Smirnov test) and are well-visualized in the form of a cumulative distribution function (figure 2F). Importantly, 40nm-GEMs showed no size variation within cells for any condition that we inspected (figure S3. These results suggest that mTORC1 controls the biophysical properties of the cytosol at the 40 nm length-scale in both yeast and mammalian cells.

mTORC1 does not affect diffusion at the length-scale of individual proteins

The change in effective diffusion of 40nm-GEMs was abundantly clear, but cellular rheology can vary considerably between particles of different sizes. Therefore, we studied other particles to check the generality and length-scale dependence of the changes in microrheology downstream of mTORC1 signaling. First, we repeated our experiments with 20nm-GEMs and found that their diffusion also increased upon mTORC1 inhibition (figure 3A). We also saw an increase in the diffusion coefficients of larger structures, including endogenous *GFA1* mRNP tagged with the PP7-GFP system (Joyner et al., 2016) and GFP-µNS particles (figure 3B-C). These structures are approximately 100 nm and 200 nm in diameter, respectively. Thus, mTORC1 modulates the effective diffusion coefficient of particles in the mesoscale, ranging from 20 nm to 200 nm in diameter.

To probe rheology at shorter length-scales, we used fluorescence correlation spectroscopy to calculate the effective diffusion of a double-GFP molecule, which is around 5 nm in diameter. The diffusion of this smaller protein was unaffected by the addition of rapamycin (figure 3D, table S1). Thus, mTORC1 inhibition increases the diffusion coefficients of particles at or above the typical size of multimeric protein complexes, but particles that are the typical size of monomeric proteins or smaller are unaffected (figure 3E).

Changes in cell cycle, translation and the cytoskeleton do not account for the effects of mTORC1 on the motion of 40nm-GEMs

Rapamycin treatment arrests cells in the G1 phase of the cell cycle. Therefore, we hypothesized that the increase in the effective diffusion coefficients of 40nm-GEMs might be due to cell cycle regulation of rheology. To test this idea, we took advantage of a chemical genetic strategy that involves inhibition of a *cdc28-as1* allele of budding yeast Cyclin Dependent Kinase 1 (Cdk1) with 1-NM-PP1 (Bishop et al., 2000). Upon complete inhibition of *Cdk1-as1* with 10 µM 1-NM-PP1, cell division arrested in G1, but no changes were observed in the motion of 40nm-GEMs (figure S2F-G. Thus, cell cycle regulation does not appear to explain the observed biophysical effects.

Protein translation is regulated by mTORC1: when nutrients and growth factors are present, cells enter an anabolic state and protein translation is upregulated in an mTORC1-dependent manner. Inhibition of mTORC1 with rapamycin leads to rapid inhibition of translation. Therefore, we tested whether decreases in translation could explain the observed changes in the effective diffusion coefficients of 40nm-GEMs. To investigate this idea, we stalled translation by addition of 1 µM cycloheximide. The median half-life of approximately 4,000 yeast proteins is about 40 minutes under these conditions (Belle et al., 2006). The motion of 40nm-GEMs was neither affected during acute cycloheximide treatment, nor after 180 minutes of treatment (figure S2F-G These results suggest that neither translational inhibition nor protein degradation explain our observations.

Another plausible hypothesis is that mTORC1 might alter the dynamics or structure of the cytoskeleton. We treated yeast cells with Latrunculin A to depolymerize the actin cytoskeleton (figure S2H) and found that, while the basal diffusion of 40nm-GEM did decrease, there was still a strong increase in D_{eff} upon rapamycin treatment. We also arrested actin dynamics in HEK293 cells using the JLY cocktail (Peng et al., 2011) (figure S2F). Similar to yeast, perturbation of actin dynamics decreased basal GEM diffusion, but the relative rapamycin effect was still similar to control conditions (figure S2H). These results suggest that the actin cytoskeleton contributes substantially to the viscosity of both the mammalian and yeast cytoplasm, but that mTORC1 does not modulate mesoscale rheology through actin-dependent effects. We then used nocodazole to depolymerize microtubules in yeast and found that the basal diffusion of 40nm-GEMs slightly increased (figure S2G. This slightly decreased the relative effect of rapamycin, but the effect magnitude was small compared to other mutants (see below). Interestingly, nocodazole treatment in mammalian cells was similar to actin in that it decreased viscosity but did not change the degree of the rapamycin-dependent diffusion increase (figure S2H). Thus, the actin and microtubule cytoskeleton play an important role in defining the mesoscale properties of the cytoplasm, but do not appear to be the primary mechanistic explanation for the regulation of rheology by mTORC1.

mTORC1 controls cytoplasmic rheology by tuning ribosome concentration

In our *S. cerevisiae* experiments, we typically observed >10 40nm-GEMs in each cell, and we imaged at ~100 Hz. In this manner, we collected thousands of traces within a few seconds. Because every cell expressed GEMs, there was no time delay associated with finding cells, and no laborious and disruptive manipulations like microinjection. These advantages enabled us to use GEMs for high-throughput screens to determine the mechanisms that control the biophysical properties of the cell.

We screened >40 candidate mutants in *S. cerevisiae* to investigate how mTORC1 might control cellular rheology (selected genes are listed in table S2). We used an *fpr1*Δ strain as a negative control. *FPR1* encodes the immunophilin protein FKBP12 that binds to rapamycin. It is the FKBP12-rapamycin complex that binds and inhibits the mTORC1 complex (Heitman et al., 1991). Thus, in the absence of the *FPR1* gene, rapamycin cannot inhibit mTORC1. In accordance with this expectation, there was no detectable effect of rapamycin on the *fpr1*Δ strain (figure 4A).

The *SIT4* gene encodes a subunit of the PP2A phosphatase required for a major signaling branch downstream of mTORC1 (Di Como and Arndt, 1996; Peterson et al., 1999). Addition of rapamycin to *sit4*Δ cells had little to no effect on particle diffusion suggesting that the change in physical properties of the cytoplasm were downstream of this gene. Together, these results validated the use of 40nm-GEMs in genetic screens and constrained our genetic screen to the PP2A-dependent branch of mTORC1-signaling.

We tested and rejected several hypotheses for the possible mechanism through which mTORC1 signaling might affect cytosolic biophysics (table S2). Eventually, we found that deletion of the *SFP1* gene, which encodes a transcription factor involved in ribosomal RNA biogenesis (Fingerman et al., 2003) increased the effective diffusion coefficient of 40nm-GEMs even more than rapamycin treatment (figure 4A, left). Furthermore, the *sfp1*Δ deletion strain led to a complete loss of the rapamycin effect (figure 4A, right). These results implicated ribosome biogenesis as a key mechanism in the control of cellular rheology.

The steady-state concentration of ribosomes in the cytoplasm is determined by the rate of ribosomal production, which is strongly affected by the *SIT4* and *SFP1* genes (Peterson et al., 1999), and the rate of ribosomal degradation. Ribosomes are usually quite stable, but starvation conditions can drive autophagy and ribophagy to accelerate rates of ribosome degradation, especially when mTORC1 is inhibited (Waliullah et al., 2017). This starvation response is thought to scavenge cellular macromolecules and organelles to recycle cellular building blocks (Reggiori and Klionsky, 2013), but reduction in the concentration of ribosomes has also been proposed as a function for these pathways (Tsukada and Ohsumi, 1993). In accordance with this latter idea, mutations in the autophagy genes *ATG1, ATG13 and ATG17* and the ribophagy gene *RIM15*

(Waliullah et al., 2017) all caused a significant decrease in the rapamycin effect (figure 4A, right).

Next, we sought to determine whether the mechanisms that we identified in *S. cerevisiae* would also hold true in mammalian cells. To this end, we employed HEK293 cells stably transduced or transfected with 40nm-GEMs and used pharmacological perturbations and siRNA to test whether ribosome concentration was important in setting the biophysical properties of mammalian cells at the 40 nm length-scale.

Inhibition of ribosome production using the small molecules BMH-21 (Peltonen et al., 2010) or CX5461 (Drygin et al., 2011) reduced the magnitude of the rapamycin effect (figure 4B, right). However, the basal diffusion coefficient only increased in CX5461 treatment (figure 4B, left). We speculate that the failure of BMH-21 to impact GEM motion could be due to off-target effects of this drug, which could lead to compensatory effects in the basal biophysical properties of the cytoplasm. Nevertheless, these pharmacological perturbations suggest that control of rRNA transcription is part of the mechanism by which mTORC1 inhibition decreases the viscosity of mammalian cells.

Stimulation of autophagy using the SMER28 compound (Tian et al., 2011), thereby reducing ribosome concentration, led to an increase in the basal diffusion of 40nm-GEMs (figure 4B, left) and strongly suppressed the effect of rapamycin (figure 4B, right). In contrast, decreasing autophagy with Wortmanin, which is predicted to increase ribosome concentration (Hansen et al., 1995), led to decreased basal diffusion (figure 4B, left). Nevertheless, this perturbation of autophagy partially blocked the effect of rapamycin (figure 4B, right).

Finally, we increased mTORC1 activity by siRNA-mediated knockdown of the mTORC1 inhibitor TSC1 (Potter et al., 2001). This treatment led to a decrease in basal diffusion (figure 3B, left, S7D). Thus, after screening over 40 mutants and drug treatments, we found that the conditions that most strongly affected the baseline of GEM diffusion and/or decreased the effect of rapamycin treatment fell into two general classes: ribosome biogenesis and autophagy.

Together, these data suggest that mTORC1 controls macromolecular crowding by tuning ribosome concentration (figure 4C).

Ribosomes act as crowding agents

Ribosomes are one of the most abundant macromolecules in the cytoplasm (Duncan and Hershey, 1983; Warner, 1999). Our genetic and pharmacological results suggested that ribosomes are the main crowding agent regulated by mTORC1. To test this hypothesis, we counted ribosomes within the native cellular environment with single molecule precision.

We used *in situ* cryo-ET to directly visualize ribosomes within the yeast cytoplasm in control and rapamycin-treated conditions. Briefly, we thinned vitreous frozen yeast cells by focused ion beam (FIB) milling (Marko et al., 2007; Rigort et al., 2012; Schaffer et al., 2017) and then performed *in situ* cryo-ET (Albert et al., 2017; Asano et al., 2016; Bykov et al., 2017; Guo et al., 2018) to produce three-dimensional images of the native cellular environment at molecular resolution (figures 5A-B, S3-S5, supplemental movies 3-4). Template matching enabled us identify ribosomes within the cellular volumes with high sensitivity (figure S4). Subsequent subtomogram averaging produced *in situ* structures of the ~30 nm ribosomes and 40nm-GEMs at 11.5 Å and 26.3 Å resolutions, respectively (figures 5C, S3-S4). In W303 yeast cells undergoing log phase growth, the concentration of ribosomes in the cytoplasm was ~14,000 ribosomes/µm^3 (23 µM), whereas this concentration decreased almost 2-fold to ~8,000 ribosomes/µm^3 (13 µM) when cells were treated with rapamycin for two hours (figure 4D). This corresponds to a drop from ribosomes occupying ~20% of the cytosolic volume to ~12%.

Ribosomes control the biophysical properties of the cytosol

Together, the screens and *in situ* cryo-ET data strongly suggest a causal relationship between ribosome concentration and the motion of particles at the 20 nm and 40 nm length-scales. We therefore developed a physical model based on the Doolittle equation to predict the effective diffusion coefficients of particles as a function of ribosome concentration (see methods, equation S5). The Doolittle equation is a phenomenological equation, meaning that there is no single theory that describes its physical origins (Doolittle, 1952). The equation was first developed to describe viscosity as a function of concentration changes that occur during polymer melts. Later Cohen and Turnbull developed a theory of hard-sphere colloids that was used to derive the Doolittle equation (Cohen and Turnbull, 1959). Thus, the equation can be used to predict the effective diffusion coefficient of a particle due to various physical changes in complex media, including the volume fraction of crowders inside the cell (figure 6A). This model is constrained by two parameters: the non-osmotic volume *v**, which is the volume occupied by all macromolecules when no further free water can be osmotically extracted from the cell, and a prefactor parameter denoted ζ which most likely relates to the degree of interaction of the tracer particle with its surrounding microenvironment.

We empirically determined both of these parameters (v* and ζ using instantaneous cell volume changes through osmotic perturbations (figure S7A-B). We found that the non-osmotic parameter is smaller for HEK293 than for *S. cerevisiae*, confirming our expectation that HEK293 cells are less crowded than yeast. The parameter ζ is very similar in both species, perhaps suggesting that 40nm-GEMs have similar interactions with the human and yeast cytosol, a result most easily explained by GEMs having very little specific interaction with their local environment. This concordance further supports the use of GEMs as a microrheological standard across organisms.

Once we had determined the parameters v* and ζ we were able to predict the effective diffusion coefficient of GEMs as a function of ribosome concentration (figure S7E-G; see methods, equation S12). We plotted this prediction for both budding yeast and mammalian cells (figure 6B-C) and found excellent agreement between our predictions and data from control conditions, rapamycin conditions and various genetic and chemical perturbations. In all cases, our model was able to accurately predict the coefficient of diffusion for GEMs over a wide range of ribosome concentrations. All parameters were experimentally determined and no data fitting was required.

We also experimentally determined the prefactor ζ for the endogenous *GFA1* messenger ribonucleoprotein complex (mRNP) tagged with the PP7-GFP system. These particles are approximately 100-200 nm in diameter. Once we determined ζ for *GFA1* mRNP particles, our model accurately predicted their effective diffusion coefficient as a function of ribosome concentration (figure S7C). Therefore, our results strongly indicate that ribosome concentration is a crucial determinant of the biophysical properties of the cytosol at length-scales of 40 to 200 nm.

mTORC1 tunes phase separation by controlling ribosome concentration

When large numbers of multivalent proteins exceed a critical nucleation concentration they can condense to form a phase-separated liquid droplet. These liquid droplets can further mature to form gels and amorphous aggregates, including pathogenic amyloid fibers and prions (Alberti and Hyman, 2016).

The phase separation of biomolecules is tuned by multiple physicochemical effects including the association and dissociation constants of interaction domains, the strength of the interaction of each molecule with the solute phase, and attraction depletion effects that can entropically favor condensation (Mourão et al., 2014). This latter effect is strongly influenced by macromolecular crowding. In addition, crowding can also affect condensation through other mechanisms, for example changes in linker lengths of multivalent proteins through solvation effects (Harmon et al., 2017). Since ribosomes are the dominant crowding agent in the cytoplasm, we hypothesized that ribosome concentration tunes phase separation. To test this idea, we took advantage of a synthetic system that is well characterized in terms of physicochemical parameters and that phase-separates into liquid droplets both *in vitro* and *in vivo.* This system is comprised of two components: ten repeats of the small ubiquitin-like modifier domain ($SUMO_{10}$)

and six repeats of SUMO interaction motif (SIM_6). The condensation of $SUMO_{10}$ and SIM_6 has been proven to be a reliable model for phase separation (Banani et al., 2016).

We assessed the effects of ribosomes on the phase separation of $SUMO_{10}$ and SIM_6. Beginning *in vitro*, we added ribosomes purified from *Escherichia coli* over a biologically-relevant concentration range determined from our cryo-ET experiments. We observed that the concentration of $SUMO_{10}$ and SIM_6 that partitioned into the condensed liquid droplet phase (partition coefficient) increased as ribosome concentrations increased. Indeed, the partition coefficient increased >50% when ribosome concentration was increased from 13 µM (mTORC1 inhibition) to 23 µM (log-phase growth) (figure 7A).

Next, we expressed an in-frame fusion of $SUMO_{10}$ and SIM_6 ($SUMO_{10}$-SIM_6) in yeast and HEK293 cells to study the effects of macromolecular crowding on phase separation *in vivo*. Due to the challenge of defining a partition-coefficient *in vivo*, we measured the total droplet area per cell as a metric of phase separation. Inhibition of mTORC1 for two hours led to an 80% and 50% decrease in $SUMO_{10}$-SIM_6 droplet area in yeast and human HEK293 cells, respectively (figure 7B). We were able to partially recover phase separation in rapamycin-treated cells by using an acute osmotic shock that reduced cell volume to an extent that restored ribosome concentrations to control levels (figure 7C, orange cross-hatched bars). The degree of phase separation is not completely recovered by osmotic compression, perhaps because this process cannot reach steady state before the osmotic shock response leads to adaptation, or because rapamycin may have effects in addition to crowding.

To further test the relationship between ribosome concentration and $SUMO_{10}$-SIM_6 condensation, while avoiding unknown effects that rapamycin may have in parallel to the change in ribosome concentration, we quantified the probability of finding a droplet in a cell as a function of ribosome concentrations in various genetic perturbations. There was a clear and strong correlation between droplet probability and ribosome concentration in this analysis (figure 7D), much stronger than the correlation between the concentration of SUMO-SIM monomers and ribosome concentration (figure S7H) or probability (figure S7I).

Taken together, these data demonstrate that ribosomes act as macromolecular crowders that tune phase separation. mTORC1 controls ribosome concentration and therefore is predicted to influence the phase separation of all cytosolic biomolecules through physicochemical effects that may include depletion attraction, solvation effects and the tuning of cell rheology.

Discussion

Recent work has reported dramatic changes in cytoplasmic rheology in response to changes in cellular energy state and metabolism. For example, depletion of ATP in *E. coli* leads to a glass-transition that greatly reduces macromolecular mobility (Parry et al., 2014), glucose starvation in yeast leads to a loss of cell volume and a decrease in the effective diffusion of mRNPs and chromosomal loci due to increased molecular crowding (Joyner et al., 2016), and decreases in cytoplasmic pH lead to a gel transition in the cytosol of yeast, associated with entry into a dormant state (Munder et al., 2016b). All of these responses increase the viscosity of the cytosol. In contrast, we show that inhibition of mTORC1 decreases the viscosity of the cytosol and protects against the putative gel transition previously described in carbon starvation. Using GEM nanoparticles, we were able to determine the mechanism for this biophysical change: ribosome concentration dominates the rheological properties of the cytoplasm at the mesoscale of tens to hundreds of nanometers. mTORC1 both drives ribosome biogenesis and decreases degradation through inhibition of autophagy (Zoncu et al., 2011). Therefore, mTORC1 regulates the physical properties of the cytoplasm by tuning the concentration of ribosomes.

Length-scale considerations in cytoplasmic viscosity have interesting implications for previous findings; for example, solidification of the yeast cytoplasm under glucose starvation was observed by tracking GFP-μNS particles, which are large condensates (Munder et al., 2016a). However, it would be surprising if the diffusion of *all* macromolecules is decreased to a solid-like state in carbon starvation. Our results show that the mobility of 40nm-GEMs is only decreased by 20% (figure S2B). This result is in agreement with the particle size dependency observed in the bacterial cytoplasm (Parry et al, 2014). In some scenarios, larger macromolecules may become spatially confined while smaller macromolecules continue to diffuse. This would lead to processes dependent on large complexes, such as apoptosis, translation or cell growth to be affected, while many basic cellular functions continue unaltered. In this way, general changes in cytoplasmic crowding could be converted into specific physiological consequences.

A major advantage of GEM nanoparticles is that they assemble into defined geometries and can therefore be used as rheological probes across multiple biological systems. We observe that GEMs have a higher diffusion coefficient in HEK293 cells than in *S. cerevisiae*, indicating that this human cell line is less crowded. Indeed, our osmotic compression experiments show a larger free water volume in HEK293 cells, consistent with this notion. In future studies, it will also be interesting to compare the physical properties of mammalian cells in different mechanical contexts, for example within tissues. Additionally, different cell types are likely to have distinct crowding, and disease mutations may lead to aberrant properties. GEMs will be a crucial tool to accelerate discovery in this area.

Beyond the diffusion coefficient, a second parameter that can be readily compared across conditions is the subdiffusive anomalous exponent, α. GEMs undergo subdiffusive motion in both cell types, but the origins of this subdiffusion remain unclear. A striking feature is that α is relatively invariant across conditions within one cell-type, but there is a species-dependent difference between yeast and human cells (figure S2I). This difference in α points to a general difference within the disordered media of the cytoplasm in these two organisms. While the physical explanation for this difference is currently unknown, there are several possibilities. Notably, mammalian cells have intermediate filaments and far more extensive actin and microtubule networks. This more elaborate cytoskeleton drives more substantial active flows and rearrangements, all of which can affect cytosolic rheology, and impose, for instance, a poroelastic response as previously described (Moeendarbary et al., 2013). Alternatively, perhaps the density and viscosity of the aqueous cytosolic medium itself varies between cell types. It has been proposed that organism-specific differences in cryo-ET image quality are due to differences in cytosolic density (Albert et al., 2017; Bykov et al., 2017), which could certainly affect α. We are excited to investigate these possibilities in the future.

Ribosomes are one of the most abundant macromolecules in the cell (around 200,000 ribosomes per yeast cell (Warner, 1999) and 3,000,000 per HeLa cell (Duncan and Hershey, 1983)), and we determined that ribosomes occupy 20% of the total volume of the yeast cytosol, thus accounting for half of the excluded volume. Indeed, when we use the phenomenological Doolittle equation to model the cytoplasm, we can accurately predict the diffusion coefficient of 40nm-GEM tracer particles and endogenous mRNPs as a function of ribosome concentration. Further study will be required to determine the precise origins of this behavior, but the biophysical properties of the cytoplasm are likely to be driven by a mixture of the colloidal effects of ribosomes as well as polymer dynamics, for example from the cytoskeleton. The predictive power of our model provides a starting point to begin to parse the relative contribution of these possible factors.

Physiological regulation of the thousands to tens of thousands of different proteins found within cells is a complex task. This regulation is achieved through finegrained mechanisms, including transcriptional and translational control of protein abundance as well as post-translational modifications such as protein phosphorylation and ubiquitylation. However, our studies suggest that macromolecular crowding could also lead to broad regulation of cell state. Changes in macromolecular crowding may provide coarse-grained regulation of protein interactions, diffusion and folding; the cell may become more solid-like in states of extreme stress, or fluidize to tune protein interactions.

Macromolecular crowding has previously been approximated by a high concentration of molecules of a wide range of sizes (Mourão et al., 2014). Our finding that ribosomes play a dominant role in setting macromolecular crowding adds an interesting caveat to this understanding: the cell *is* crowded by proteins of a large variety of sizes, and there is likely no dominant crowder at the scale of individual proteins, but the crowding environment around large macromolecular complexes is set by ribosome concentration.

It has long been understood that molecular crowding is crucial for biological systems. Our work begins to elucidate why. We show that changes in ribosomal crowding tune phase separation both *in vitro* and *in vivo*. The effects on phase separation in our system could be attributed to several possible causes including attraction depletion effects (Woodruff et al., 2015) and solvation impacts on the linkers in our polyvalent model system (Harmon et al., 2017). Regardless of mechanism, our finding implies that mTORC1, and indeed any signaling pathway that alters the steady-state concentration of ribosomes, will control the phase separation of every biological condensate. Thus, our work provides insight relevant to the burgeoning field of phase separation of cytosolic biomolecular condensates. Interest in this topic is rapidly growing, as investigators elucidate the impacts of phase separation on proteins involved in many fundamental processes such as photosynthesis (Freeman Rosenzweig et al., 2017), cell division (Woodruff et al., 2017), development (Brangwynne et al., 2009), learning (Si et al., 2010), immune signaling (Cai et al., 2014; Hou et al., 2011), and human pathologies including cancer (Kwon et al., 2013), aging and neurodegeneration (Jain and Vale, 2017; Kwon et al., 2014).

References and Notes:

Akita, F., Chong, K.T., Tanaka, H., Yamashita, E., Miyazaki, N., Nakaishi, Y., Suzuki, M., Namba, K., Ono, Y., Tsukihara, T., et al. (2007). The crystal structure of a virus-like particle from the hyperthermophilic archaeon Pyrococcus furiosus provides insight into the evolution of viruses. J Mol Biol *368*, 1469–1483.

Albert, S., Schaffer, M., Beck, F., Mosalaganti, S., Asano, S., Thomas, H.F., Plitzko, J.M., Beck, M., Baumeister, W., and Engel, B.D. (2017). Proteasomes tether to two distinct sites at the nuclear pore complex. Proceedings of the National Academy of Sciences *114*, 13726–13731.

Alberti, S., and Hyman, A.A. (2016). Are aberrant phase transitions a driver of cellular aging? Bioessays *38*, 959–968.

Asano, S., Engel, B.D., and Baumeister, W. (2016). In Situ Cryo-Electron Tomography: A Post-Reductionist Approach to Structural Biology (Academic Press).

Banani, S.F., Rice, A.M., Peeples, W.B., Lin, Y., Jain, S., Parker, R., and Rosen, M.K. (2016). Compositional Control of Phase-Separated Cellular Bodies. Cell *166*, 651–663.

Belle, A., Tanay, A., Bitincka, L., Shamir, R., and O'Shea, E.K. (2006). Quantification of protein half-lives in the budding yeast proteome. Proc Natl Acad Sci USA *103*, 13004–13009.

Bharat, T.A.M., Russo, C.J., Löwe, J., Passmore, L.A., and Scheres, S.H.W. (2015). Advances in Single-Particle Electron Cryomicroscopy Structure Determination applied to Sub-tomogram Averaging. Structure *23*, 1743–1753.

Bishop, A.C., Ubersax, J.A., Petsch, D.T., Matheos, D.P., Gray, N.S., Blethrow, J., Shimizu, E., Tsien, J.Z., Schultz, P.G., Rose, M.D., et al. (2000). A chemical switch for inhibitor-sensitive alleles of any protein kinase. Nature *407*, 395–401.

Brangwynne, C.P., Eckmann, C.R., Courson, D.S., Rybarska, A., Hoege, C., Gharakhani, J., Jülicher, F., and Hyman, A.A. (2009). Germline P granules are liquid droplets that localize by controlled dissolution/condensation. *324*, 1729–1732.

Brazda, P., Szekeres, T., Bravics, B., Tóth, K., Vámosi, G., and Nagy, L. (2011). Live-cell fluorescence correlation spectroscopy dissects the role of coregulator exchange and chromatin binding in retinoic acid receptor mobility. J Cell Sci *124*, 3631–3642.

Broering, T.J., Arnold, M.M., Miller, C.L., Hurt, J.A., Joyce, P.L., and Nibert, M.L. (2005). Carboxyl-proximal regions of reovirus nonstructural protein muNS necessary and sufficient for forming factory-like inclusions. J Virol *79*, 6194–6206.

Bykov, Y.S., Schaffer, M., Dodonova, S.O., Albert, S., Plitzko, J.M., Baumeister, W., Engel, B.D., and Briggs, J.A. (2017). The structure of the COPI coat determined within the cell. Elife *6*, 6916.

Cai, X., Chen, J., Xu, H., Liu, S., Jiang, Q.-X., Halfmann, R., and Chen, Z.J. (2014). Prion-like polymerization underlies signal transduction in antiviral immune defense and inflammasome activation. Cell *156*, 1207–1222.

Chen, Y., Pfeffer, S., Hrabe, T., Schuller, J.M., and Förster, F. (2013). Fast and accurate reference-free alignment of subtomograms. Journal of Structural Biology *182*, 235–245.

Cohen, M.H., and Turnbull, D. (1959). Molecular transport in liquids and glasses. The Journal of Chemical Physics *31*, 1164–1169.

Daniels, B.R., Masi, B.C., and Wirtz, D. (2006). Probing single-cell micromechanics in vivo: the microrheology of C. elegans developing embryos. Biophys J *90*, 4712–4719.

Di Como, C.J., and Arndt, K.T. (1996). Nutrients, via the Tor proteins, stimulate the association of Tap42 with type 2A phosphatases. Genes Dev *10*, 1904–1916.

Doolittle, A.K. (1952). Studies in Newtonian flow. III. The dependence of the viscosity of liquids on molecular weight and free space (in homologous series). Journal of Applied Physics *23*, 236–239.

Drygin, D., Lin, A., Bliesath, J., Ho, C.B., O'Brien, S.E., Proffitt, C., Omori, M., Haddach, M., Schwaebe, M.K., Siddiqui-Jain, A., et al. (2011). Targeting RNA polymerase I with an oral small molecule CX-5461 inhibits ribosomal RNA synthesis and solid tumor growth. Cancer Res *71*, 1418–1430.

Duncan, R., and Hershey, J.W. (1983). Identification and quantitation of levels of protein synthesis initiation factors in crude HeLa cell lysates by two-dimensional polyacrylamide gel electrophoresis. J Biol Chem *258*, 7228–7235.

Eibauer, M., Hoffmann, C., Plitzko, J.M., Baumeister, W., Nickell, S., and Engelhardt, H. (2012). Unraveling the structure of membrane proteins in situ by transfer function corrected cryo-electron tomography. Journal of Structural Biology *180*, 488–496.

Fingerman, I., Nagaraj, V., Norris, D., and Vershon, A.K. (2003). Sfp1 plays a key role in yeast ribosome biogenesis. Eukaryotic Cell *2*, 1061–1068.

Förster, F., and Hegerl, R. (2007). Structure Determination In Situ by Averaging of Tomograms. Methods Cell Biol *79*, 741–767.

Frangakis, A.S., Böhm, J., Förster, F., Nickell, S., Nicastro, D., Typke, D., Hegerl, R., and Baumeister, W. (2002). Identification of macromolecular complexes in cryoelectron tomograms of phantom cells. Proc Natl Acad Sci USA *99*, 14153–14158.

Freeman Rosenzweig, E.S., Xu, B., Kuhn Cuellar, L., Martinez-Sanchez, A., Schaffer, M., Strauss, M., Cartwright, H.N., Ronceray, P., Plitzko, J.M., Förster, F., et al. (2017).

The Eukaryotic CO2-Concentrating Organelle Is Liquid-like and Exhibits Dynamic Reorganization. Cell *171*, 148–162.e19.

Goddard, T.D., Huang, C.C., and Ferrin, T.E. (2007). Visualizing density maps with UCSF Chimera. Journal of Structural Biology *157*, 281–287.

Grabocka, E., and Bar-Sagi, D. (2016). Mutant KRAS Enhances Tumor Cell Fitness by Upregulating Stress Granules. Cell *167*, 1803–1813.e1812.

Guo, Q., Lehmer, C., Martinez-Sanchez, A., Rudack, T., Beck, F., Hartmann, H., Pérez-Berlanga, M., Frottin, F., Hipp, M.S., Hartl, F.U., et al. (2018). In Situ Structure of Neuronal C9orf72 Poly-GA Aggregates Reveals Proteasome Recruitment. Cell *172*, 696–705.e12.

Hansen, S.H., Olsson, A., and Casanova, J.E. (1995). Wortmannin, an inhibitor of phosphoinositide 3-kinase, inhibits transcytosis in polarized epithelial cells. J Biol Chem *270*, 28425–28432.

Hara, K., Yonezawa, K., Weng, Q.P., Kozlowski, M.T., Belham, C., and Avruch, J. (1998). Amino acid sufficiency and mTOR regulate p70 S6 kinase and eIF-4E BP1 through a common effector mechanism. Journal of Biological Chemistry *273*, 14484–14494.

Harmon, T.S., Holehouse, A.S., Rosen, M.K., and Pappu, R.V. (2017). Intrinsically disordered linkers determine the interplay between phase separation and gelation in multivalent proteins. Elife *6*, 5.

Heitman, J., Movva, N.R., and Hall, M.N. (1991). Targets for cell cycle arrest by the immunosuppressant rapamycin in yeast. *253*, 905–909.

Hou, F., Sun, L., Zheng, H., Skaug, B., Jiang, Q.-X., and Chen, Z.J. (2011). MAVS forms functional prion-like aggregates to activate and propagate antiviral innate immune response. Cell *146*, 448–461.

Hrabe, T., Chen, Y., Pfeffer, S., Kuhn Cuellar, L., Mangold, A.-V., and Förster, F. (2012). PyTom: A python-based toolbox for localization of macromolecules in cryo-electron tomograms and subtomogram analysis. Journal of Structural Biology *178*, 177–188.

Jain, A., and Vale, R.D. (2017). RNA phase transitions in repeat expansion disorders. Nature *546*, 243–247.

Joyner, R.P., Tang, J.H., Helenius, J., Dultz, E., Brune, C., Holt, L.J., Huet, S., Müller, D.J., and Weis, K. (2016). A glucose-starvation response regulates the diffusion of macromolecules. Elife *5*.

Kaganovich, D., Kopito, R., and Frydman, J. (2008). Misfolded proteins partition between two distinct quality control compartments. Nature *454*, 1088–1095.

Kwon, I., Kato, M., Xiang, S., Wu, L., Theodoropoulos, P., Mirzaei, H., Han, T., Xie, S., Corden, J.L., and McKnight, S.L. (2013). Phosphorylation-Regulated Binding of RNA Polymerase II to Fibrous Polymers of Low-Complexity Domains. Cell *155*, 1049–1060.

Kwon, I., Xiang, S., Kato, M., Wu, L., Theodoropoulos, P., Wang, T., Kim, J., Yun, J., Xie, Y., and McKnight, S.L. (2014). Poly-dipeptides encoded by the C9orf72 repeats bind nucleoli, impede RNA biogenesis, and kill cells. *345*, 1139–1145.

Lohka, M.J., and Maller, J.L. (1985). Induction of nuclear envelope breakdown, chromosome condensation, and spindle formation in cell-free extracts. J Cell Biol *101*, 518–523.

Luby-Phelps, K., Taylor, D.L., and Lanni, F. (1986). Probing the structure of cytoplasm. Journal of Cell Biology *102*, 2015–2022.

Marko, M., Hsieh, C., Schalek, R., Frank, J., and Mannella, C. (2007). Focused-ion-beam thinning of frozen-hydrated biological specimens for cryo-electron microscopy. Nat Meth *4*, 215–217.

Mastronarde, D.N. (2005). Automated electron microscope tomography using robust prediction of specimen movements. Journal of Structural Biology *152*, 36–51.

Miermont, A., Waharte, F., Hu, S., McClean, M.N., Bottani, S., Léon, S., and Hersen, P. (2013). Severe osmotic compression triggers a slowdown of intracellular signaling, which can be explained by molecular crowding. Proceedings of the National Academy of Sciences *110*, 5725–5730.

Moeendarbary, E., Valon, L., Fritzsche, M., Harris, A.R., Moulding, D.A., Thrasher, A.J., Stride, E., Mahadevan, L., and Charras, G.T. (2013). The cytoplasm of living cells behaves as a poroelastic material. Nat Mater *12*, 253–261.

Mourão, M.A., Hakim, J.B., and Schnell, S. (2014). Connecting the dots: the effects of macromolecular crowding on cell physiology. Biophys J *107*, 2761–2766.

Munder, M.C., Midtvedt, D., Franzmann, T., Nüske, E., Otto, O., Herbig, M., Ulbricht, E., Müller, P., Taubenberger, A., Maharana, S., et al. (2016a). A pH-driven transition of the cytoplasm from a fluid- to a solid-like state promotes entry into dormancy. Elife *5*, e09347.

Munder, M.C., Midtvedt, D., Franzmann, T., Nüske, E., Otto, O., Herbig, M., Ulbricht, E., Müller, P., Taubenberger, A., Maharana, S., et al. (2016b). A pH-driven transition of the cytoplasm from a fluid- to a solid-like state promotes entry into dormancy. Elife *5*, e09347.

Nickell, S., Förster, F., Linaroudis, A., Net, W.D., Beck, F., Hegerl, R., Baumeister, W., and Plitzko, J.M. (2005). TOM software toolbox: acquisition and analysis for electron tomography. Journal of Structural Biology *149*, 227–234.

Parry, B.R., Surovtsev, I.V., Cabeen, M.T., O'Hern, C.S., Dufresne, E.R., and Jacobs-Wagner, C. (2014). The bacterial cytoplasm has glass-like properties and is fluidized by metabolic activity. Cell *156*, 183–194.

Peltonen, K., Colis, L., Liu, H., Jäämaa, S., Moore, H.M., Enbäck, J., Laakkonen, P., Vaahtokari, A., Jones, R.J., af Hällström, T.M., et al. (2010). Identification of Novel p53 Pathway Activating Small-Molecule Compounds Reveals Unexpected Similarities with Known Therapeutic Agents. PLoS ONE *5*, e12996.

Peng, G.E., Wilson, S.R., and Weiner, O.D. (2011). A pharmacological cocktail for arresting actin dynamics in living cells. Mol Biol Cell *22*, 3986–3994.

Peterson, R.T., Desai, B.N., Hardwick, J.S., and Schreiber, S.L. (1999). Protein phosphatase 2A interacts with the 70-kDa S6 kinase and is activated by inhibition of FKBP12-rapamycinassociated protein. Proc Natl Acad Sci USA *96*, 4438–4442.

Petrášek, Z., and Schwille, P. (2008). Precise Measurement of Diffusion Coefficients using Scanning Fluorescence Correlation Spectroscopy. Biophys J *94*, 1437–1448.

Potter, C.J., Huang, H., and Xu, T. (2001). Drosophila Tsc1 functions with Tsc2 to antagonize insulin signaling in regulating cell growth, cell proliferation, and organ size. Cell *105*, 357–368.

Reggiori, F., and Klionsky, D.J. (2013). Autophagic processes in yeast: mechanism, machinery and regulation. Genetics *194*, 341–361.

Rigort, A., Bäuerlein, F.J.B., Villa, E., Eibauer, M., Laugks, T., Baumeister, W., and Plitzko, J.M. (2012). Focused ion beam micromachining of eukaryotic cells for cryoelectron tomography. Proceedings of the National Academy of Sciences *109*, 4449–4454.

Rivas, G., Fernández, J.A., and Minton, A.P. (2001). Direct observation of the enhancement of noncooperative protein self-assembly by macromolecular crowding: indefinite linear self-association of bacterial cell division protein FtsZ. Proc Natl Acad Sci USA *98*, 3150–3155.

Russell, W.C., Graham, F.L., Smiley, J., and Nairn, R. (1977). Characteristics of a Human Cell Line Transformed by DNA from Human Adenovirus Type 5. J. Gen. Virol. *36*, 59–72.

Schaffer, M., Mahamid, J., Engel, B.D., Laugks, T., Baumeister, W., and Plitzko, J.M. (2017). Optimized cryo-focused ion beam sample preparation aimed at in situ structural studies of membrane proteins. Journal of Structural Biology *197*, 73–82.

Shav-Tal, Y., Darzacq, X., Shenoy, S.M., Fusco, D., Janicki, S.M., Spector, D.L., and Singer, R.H. (2004). Dynamics of Single mRNPs in Nuclei of Living Cells. *304*, 1797–1800.

Si, K., Choi, Y.-B., White-Grindley, E., Majumdar, A., and Kandel, E.R. (2010). Aplysia CPEB can form prion-like multimers in sensory neurons that contribute to long-term facilitation. Cell *140*, 421–435.

Slaughter, B.D., Schwartz, J.W., and Li, R. (2007). Mapping dynamic protein interactions in MAP kinase signaling using live-cell fluorescence fluctuation spectroscopy and imaging. Proceedings of the National Academy of Sciences *104*, 20320–20325.

Su, X., Ditlev, J.A., Hui, E., Xing, W., Banjade, S., Okrut, J., King, D.S., Taunton, J., Rosen, M.K., and Vale, R.D. (2016). Phase separation of signaling molecules promotes T cell receptor signal transduction. Science *352*, 595–599.

Tian, Y., Bustos, V., Flajolet, M., and Greengard, P. (2011). A small-molecule enhancer of autophagy decreases levels of Abeta and APP-CTF via Atg5-dependent autophagy pathway. Faseb J *25*, 1934–1942.

Trappe, V., Prasad, V., Cipelletti, L., Segre, P.N., and Weitz, D.A. (2001). Jamming phase diagram for attractive particles. Nature *411*, 772–775.

Tsukada, M., and Ohsumi, Y. (1993). Isolation and characterization of autophagy-defective mutants of Saccharomyces cerevisiae. FEBS Lett *333*, 169–174.

Waliullah, T.M., Yeasmin, A.M., Kaneko, A., Koike, N., Terasawa, M., Totsuka, T., and Ushimaru, T. (2017). Rim15 and Sch9 kinases are involved in induction of autophagic degradation of ribosomes in budding yeast. Biosci Biotechnol Biochem *81*, 307–310.

Wang, B., Kuo, J., Bae, S.C., and Granick, S. (2012). When Brownian diffusion is not Gaussian. Nat Mater *11*, 481–485.

Warner, J.R. (1999). The economics of ribosome biosynthesis in yeast. Trends Biochem Sci *24*, 437–440.

Wirtz, D. (2009). Particle-tracking microrheology of living cells: principles and applications. Annu Rev Biophys *38*, 301–326.

Woodruff, J.B., Ferreira Gomes, B., Widlund, P.O., Mahamid, J., Honigmann, A., and Hyman, A.A. (2017). The Centrosome Is a Selective Condensate that Nucleates Microtubules by Concentrating Tubulin. Cell *169*, 1066–1077.e10.

Woodruff, J.B., Wueseke, O., Viscardi, V., Mahamid, J., Ochoa, S.D., Bunkenborg, J., Widlund, P.O., Pozniakovsky, A., Zanin, E., Bahmanyar, S., et al. (2015). Centrosomes. Regulated assembly of a supramolecular centrosome scaffold in vitro. *348*, 808–812.

Zapata-Hommer, O., and Griesbeck, O. (2003). Efficiently folding and circularly permuted variants of the Sapphire mutant of GFP. BMC Biotechnology *3*, 5.

Zhang, X., Meining, W., Fischer, M., Bacher, A., and Ladenstein, R. (2001). X-ray structure analysis and crystallographic refinement of lumazine synthase from the hyperthermophile Aquifex aeolicus at 1.6 A resolution: determinants of thermostability revealed from structural comparisons. J Mol Biol *306*, 1099–1114.

Zheng, S.Q., Palovcak, E., Armache, J.-P., Verba, K.A., Cheng, Y., and Agard, D.A. (2017). MotionCor2: anisotropic correction of beam-induced motion for improved cryo-electron microscopy. Nat Meth *14*, 331–332.

Zhou, H.-X., Rivas, G., and Minton, A.P. (2008). Macromolecular crowding and confinement: biochemical, biophysical, and potential physiological consequences. Annu Rev Biophys *37*, 375–397.

Zoncu, R., Efeyan, A., and Sabatini, D.M. (2011). mTOR: from growth signal integration to cancer, diabetes and ageing. Nat. Rev. Mol. Cell Biol. *12*, 21–35.

Acknowledgements:

We thank Christophe Renou for initial contributions to this project and Monatrice Lam for additional help with FCS measurements. We thank David Savage for initial suggestions about how to build GEMs. We thank David Morgan, David Drubin, Karsten Weis, Jeremy Thorner, Mike Rosen, Amy Gladfelter, Jef Boeke and Douglas Koshland for advice, strains, plasmids and reagents.

We thank William Ludington, Jasna Brujic, Mike Rosen, Jitu Mayor, Ron Vale, Jim Wilhelm, Marcus Taylor, Jan von Skotheim, Josh Zimmerberg for discussions; and Emily Adney, David Truong, Jef Boeke, John Gerhart, Fred Wilt, Ryan Joyner, Carlos Pantoja, Tim Lionnett, Jon Ditlev, Matthew Maurano, Gabrielle Riekhoff, for help with the manuscript.

We acknowledge the help and support of the Janelia Advanced Imaging Center, a facility jointly supported by the Gordon and Betty Moore Foundation and HHMI at HHMI's Janelia Research Campus in collecting 3D data using the aberration corrected multifocal microscope – data necessary to validate our 2D simplifications.

We thank NYULMC DART Microscopy Laboratory for the consultation and assistance with TEM work.

We gratefully acknowledge funding from the William Bowes Fellows program, the Vilcek Foundation, and the HHMI HCIA summer institute (LJH); the National Science Foundation Graduate Research Fellows Program (GB). Christine Jacobs-Wagner is an Investigator of the Howard Hughes Medical Institute.

Data Availability:

All subtomogram averages presented in this study have been deposited in the Electron Microscopy Data Bank (EMD-XXXX, EMD-XXXX, EMD-XXXX, EMD-XXXX), along with the tomograms from Figure 4 (EMD-XXXX, EMD-XXXX).

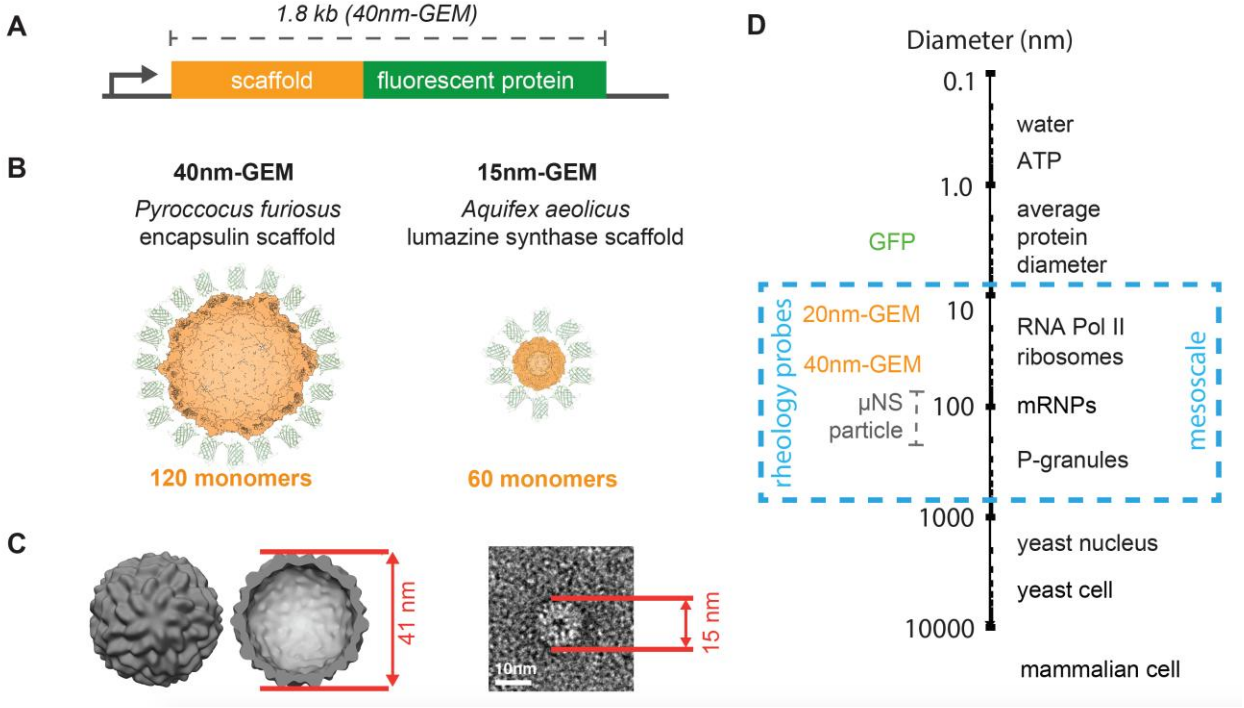

Figure 1. Genetically Encoded Multimeric nanoparticles (GEMs) are homomultimeric fluorescent nanoparticles that self-assemble to a stereotyped size and shape. (**A**) General gene structure of GEMs, which consist of an in-frame fusion of a multimerizing scaffold to a fluorescent protein. (**B**) Predicted structures of 40nm-GEMs and 20nm-GEMs. (**C**) Left, cryo-ET subtomogram average of 40nm-GEMs within the cell; Right, averaged negative stain EM images of 20nm-GEMs. (**D**) Diameters of GEMs and other macromolecules at the meso length-scale, shown in relation to small molecules, protein complexes, and cells.

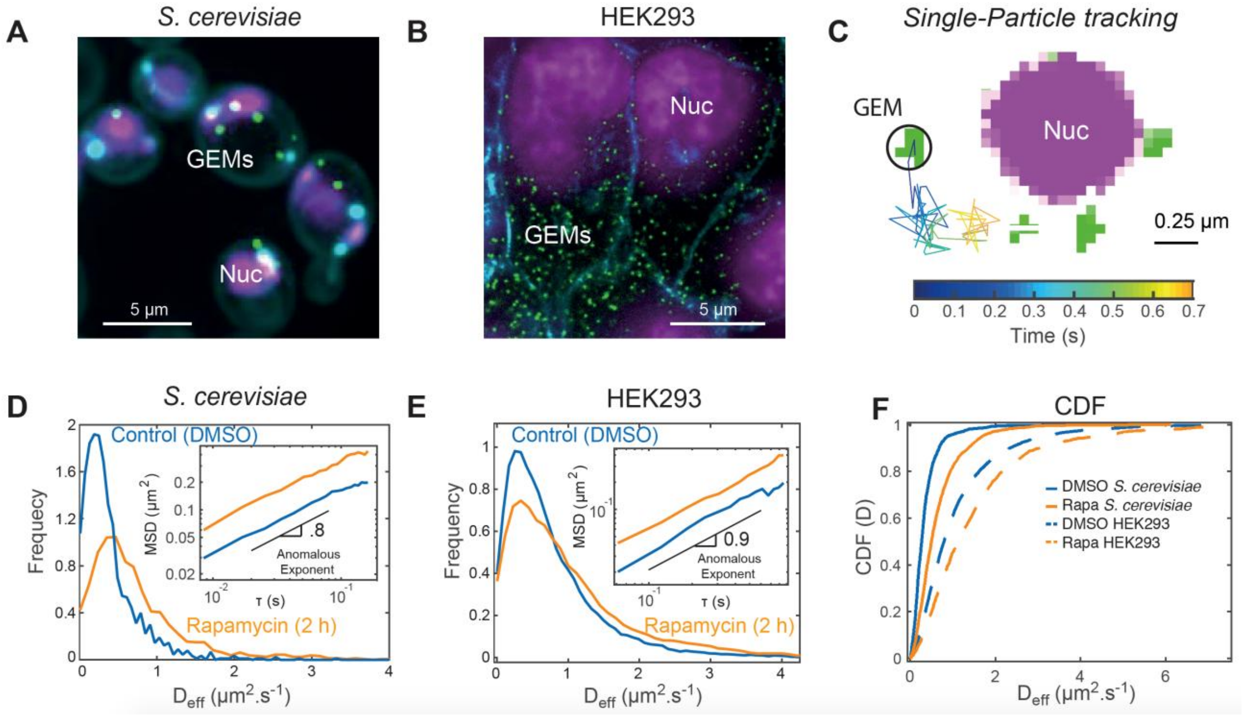

Figure 2. mTORC1 inhibition increases the effective diffusion coefficient of GEMs. (**A**) 40nm-GEMs expressed in (**A**) *S. cerevisiae* and (**B**) HEK293 cells. GEMs are visualized using a T-Sapphire fluorescent protein (green). DNA is visualized with SiR-Hoeschst (magenta). Yeast cell walls and mitochondria were visualized using calcofluor-white and HEK293 membrane with wheat germ agglutinin (cyan). (**C**) High magnification example of tracking of a 40-nm GEM particle (green) within an *S. cerevisiae* cell, imaging at 100 frames per second. Three other GEMs and the nucleus (magenta) are also displayed. (**D-E**) Distribution of 40nm-GEM effective diffusion coefficients (D_{eff}) for *S. cerevisiae* (**D**) and HEK293 (**E**); results from DMSO (carrier control) treatment are displayed in blue; rapamycin treatment results are displayed in orange. Insets: time and ensemble-averaged mean-square displacements in log-log space with the anomalous exponent indicated. (**F**) Cumulative distribution function showing D_{eff} da-

ta for both *S. cerevisiae* (solid lines) and HEK293 cells (dashed lines) in both control (blue) and rapamycin treatment (orange).

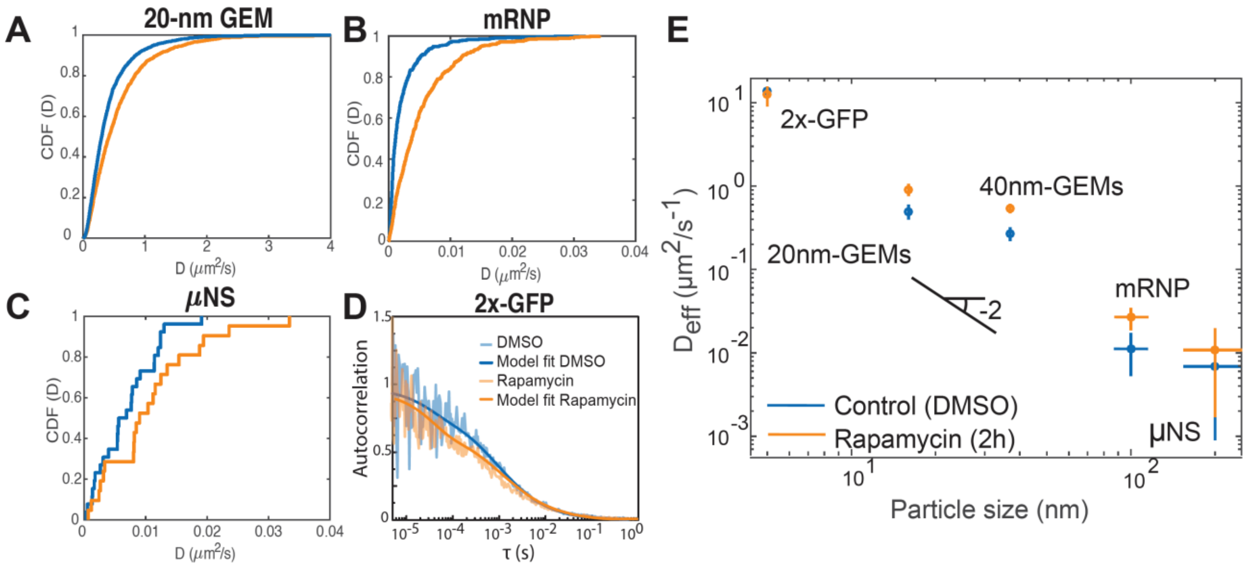

Figure 3. mTORC1 inhibition increases the effective diffusion of particles 20 nm and larger in *S. cerevisiae*. (**A-C**) Cumulative distribution plots showing D_{eff} data for 20nm-GEMs (**A**), *GFA1* mRNP particles (**B**), and µNS inclusion (**C**). (**D**) Fluorescence correlation spectroscopy (FCS) autocorrelation function for a tandem GFP dimer (stokes radius approximately 5 nm) (**E**) Effect of rapamycin on the effective diffusion coefficients of endogenous molecules and tracer particles of various sizes. Indicated, the -2 power-law scaling of diffusion coefficient as a function of diameter, which does not conform to Stokes-Einstein predictions. In all cases control conditions are shown in blue and rapamycin in orange.

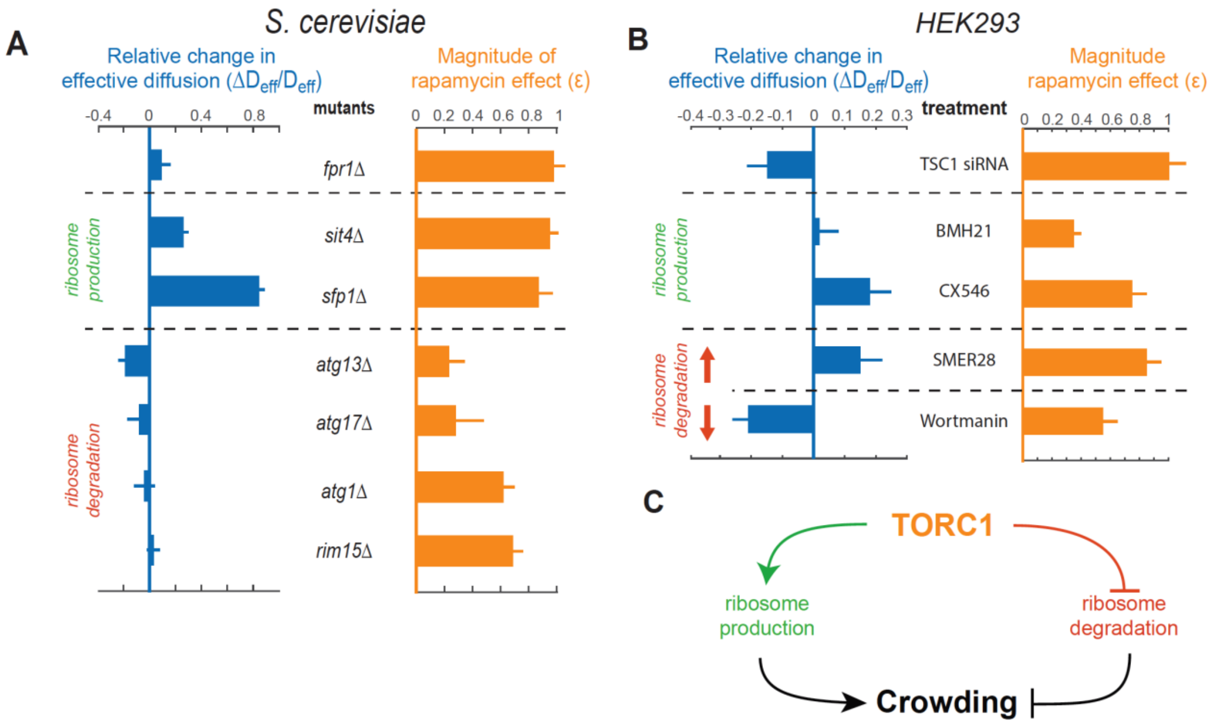

Figure 4. mTORC1 controls the effective diffusion coefficient of 40nm-GEMs by tuning ribosome concentration. (**A**) Selected mutants from a candidate screen in *S. cerevisiae.* The change in the baseline effective diffusion coefficients of 40nm-GEMs (left, blue) is plotted for each mutant; along with the magnitude of the rapamycin effect (right, orange). (**B**) Pharmacological and siRNA perturbations in HEK293 cells suggest that mTORC1 also modulates cytoplasmic rheology through ribosome crowding in mammals. Data are presented as the median +/- SEM (standard error of the mean). (**C**) Proposed model of crowding control in *S. cerevisiae* and HEK293 cells.

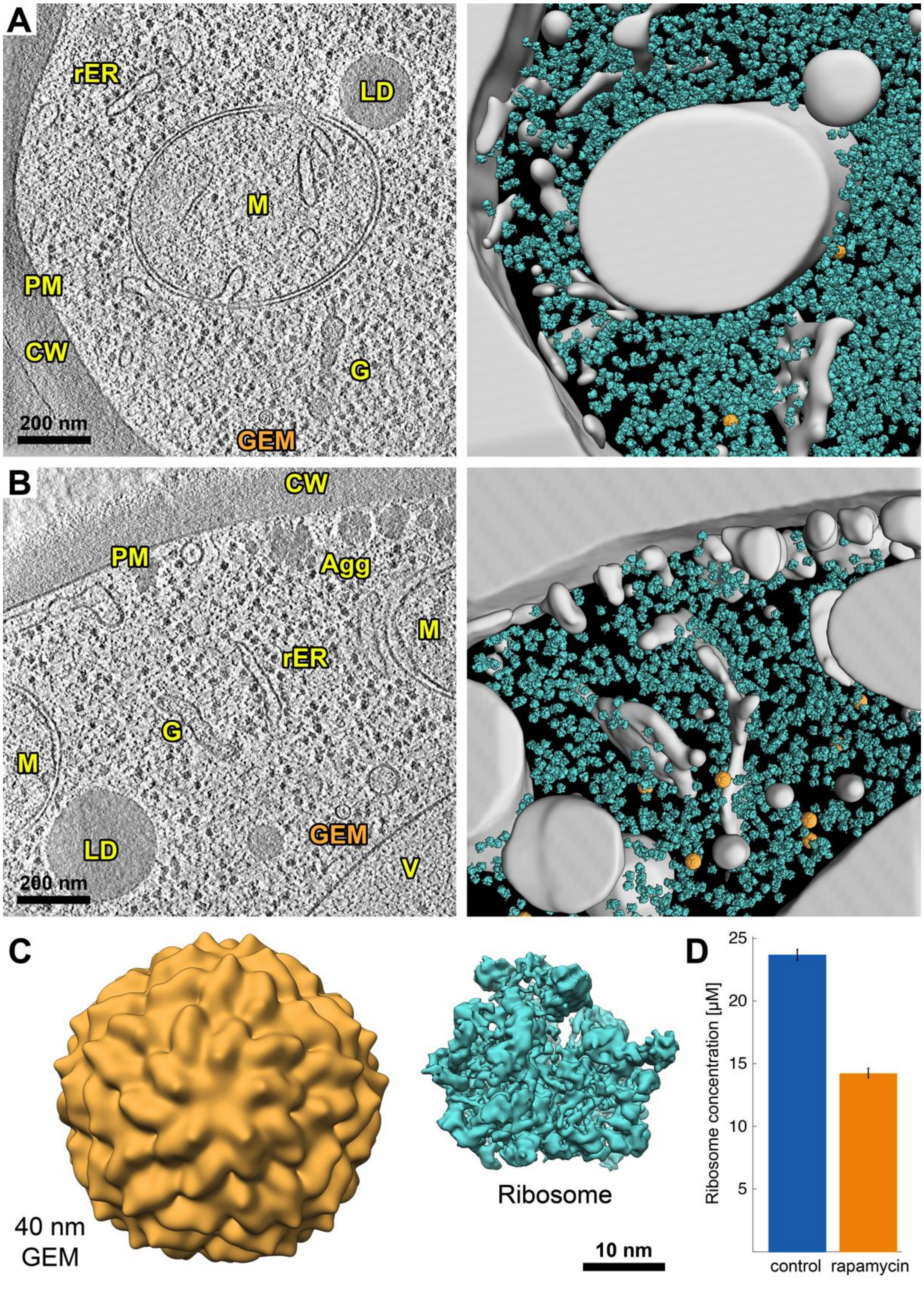
A
rER
LD
M
PM
CW
G
200 nm
GEM
B
CW
PM
Agg
M
rER
G
M
LD
GEM
V
200 nm
C
40 nm
GEM
Ribosome
10 nm
D
Ribosome concentration [µM]
25
20
15
10
5
control
rapamycin

Figure 5. *In situ* cryo-electron tomography of FIB-milled *S. cerevisiae* reveals that ribosome concentration dramatically decreases upon mTORC1 inhibition. (**A**) DMSO-treated cells. (**B**) Rapamycin-treated cells. (**Left**) Slice through a representative cryo-electron tomogram of a FIB-milled yeast cell. The cell wall (CW), plasma membrane (PM), rough endoplasmic reticulum (rER), lipid droplets (LD), mitochondria (M), Golgi apparatus (G), vacuole (V), aggregates (Agg), and one example GEM nanoparticle are indicated. (**Right**) 3D segmentation of the same tomogram showing ribosomes (cyan) and GEMs (orange). The non-cytosolic volume is grey. (**C**) Subtomogram averages of the 40nm-GEM nanoparticles and ~30 nm ribosomes from within the cellular volumes, shown in relative proportion. (**D**) Cytosolic ribosome concentrations after 2 h DMSO (blue) and rapamycin (orange) treatment. Error bars are SEM. Concentrations were calculated from 14 DMSO-treated and 13 rapamycin-treated cells (see Figs. S5 and S6).

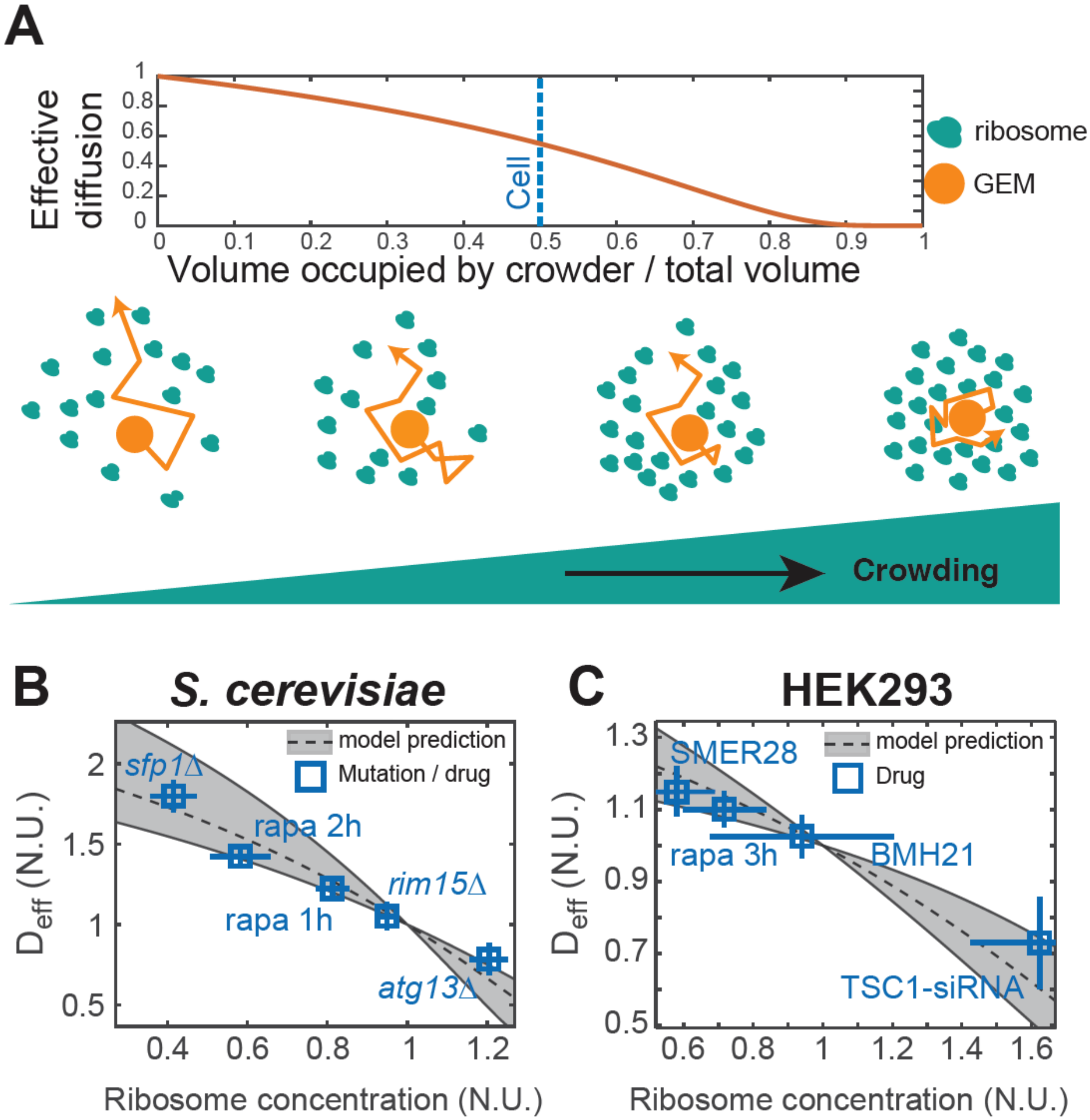

Figure 6. A physical model of the cytosol accurately predicts diffusion as a function of ribosome concentration. (**A**) The phenomenological Doolittle equation describes the effective diffusion coefficient of particles as a function of excluded volume. (**B** and **C**) A model based on the Doolittle equation, and parameterized empirically with no fitted parameters, accurately predicts the diffusion coefficient of 40nm-GEMs in both

yeast (**B**) and HEK293 cells (**C**) as a function of the concentration of ribosomes (measured by quantification of a total extracted nucleic acids, see figure S8E-G.) Median coefficients of diffusion are normalized to WT conditions on the day the data was acquired and plotted as the median +/- SEM. Prediction is shown as a dashed black line with grey confidence intervals based on the error associated with the estimation of ζ.

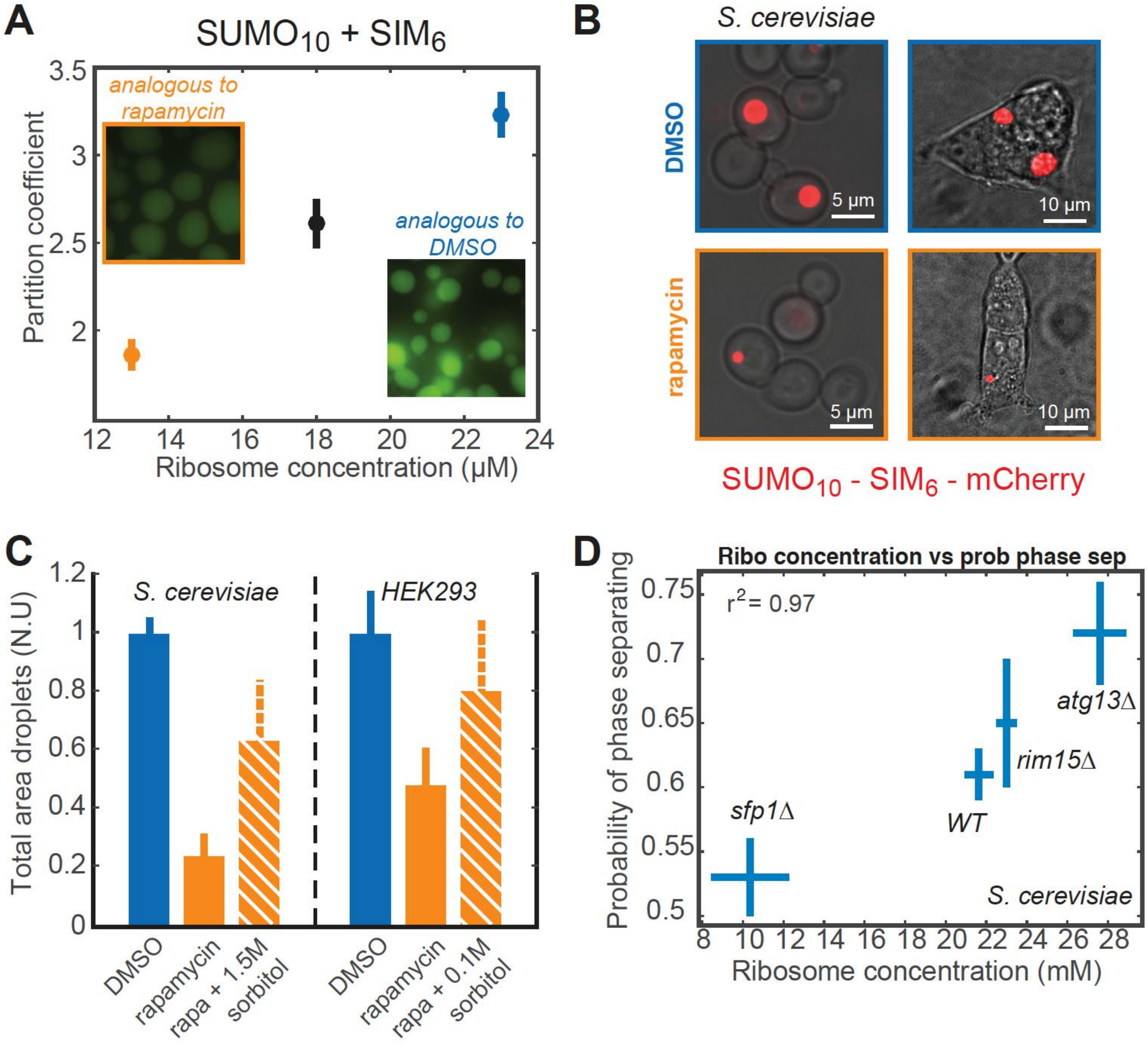

Figure 7. Ribosomes act as a crowding agent that drives phase separation both *in vitro* and *in vivo*. (**A**) A homodecamer repeat of SUMO (SUMO$_{10}$) was mixed with a homohexamer repeat **S**umo **I**nteraction **M**otif peptide (**SIM**$_6$) to achieve equimolar concentrations of each monomer (60 µM). SUMO$_{10}$ + SIM$_6$ was kept at constant concentration and incubated with an increasing concentration of fully assembled 70S ribosomes (purified from *E. coli*). There was a >50% increase in the partition coefficient of SUMO$_{10}$ + SIM$_6$ when ribosome concentration was increased from 13 µM (equivalent to yeast

treated with rapamycin) to 23 µM (the concentration of ribosomes in logarithmically growing yeast cells). (**B**) An in-frame fusion of $SUMO_{10}$-SIM_6-GFP was expressed in budding yeast (*S. cerevisiae* W303) and HEK293 cells. Micrographs of control cells (DMSO) and cells treated with rapamycin for 2 h. (**C**) Quantification of total area of phase-separated droplets in control cells (blue), cells treated with rapamycin (orange), and cells treated with rapamycin followed with a hyperosmotic shock with 1.5M (yeast cells) or 0.1M (human cells) sorbitol (orange bars with white cross hatches). (**D**) Probability of observing $Sumo_{10}$-SIM_6 phase separation versus ribosome concentration in ribosomal crowding mutants *sfp1*Δ, *rim15*Δ*, and atg13*Δ as well as WT BY4741.

Supplemental Figures

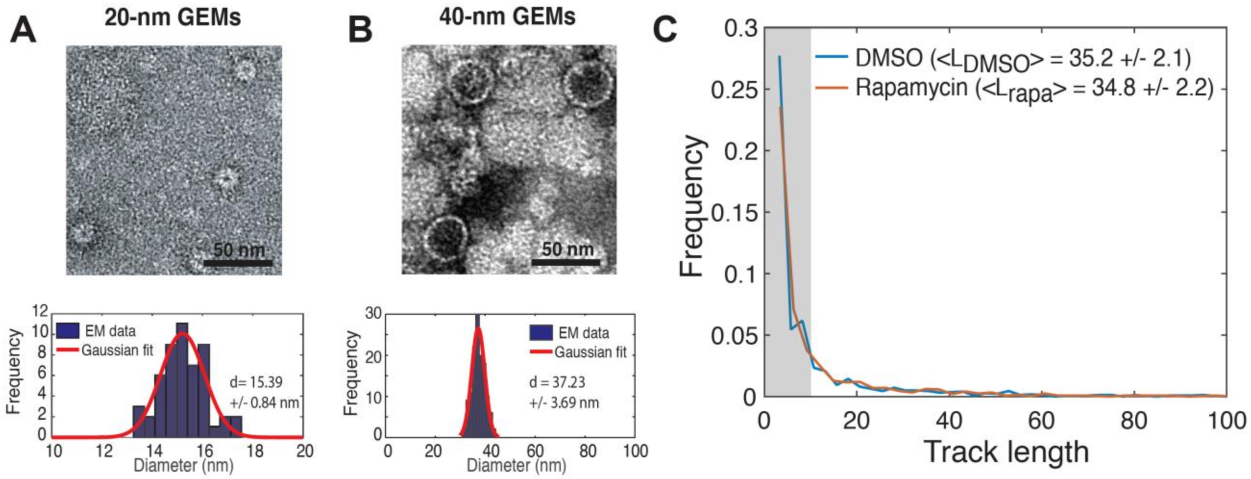

Figure S1: Negative-stain EM of 40-nm and 20-nm GEMs and track length histogram. Related to figures 1 and 2. (**A**) 20-nm GEMs are seen to be 15.39 +/- 0.84 nm by negative stain EM. (**B**) 40-nm GEMs, which are seen to be 41 nm in high accurate *in-situ* cryo-EM tomography are appear to be 37.23 +/- 3.69nm by negative stain EM. (**C**) The median track length for 40-nm GEMs in DMSO and Rapamycin treatment is similar at 35.2 +/- 2.1 and 34.8 +/- 2.2 frames, respectively.

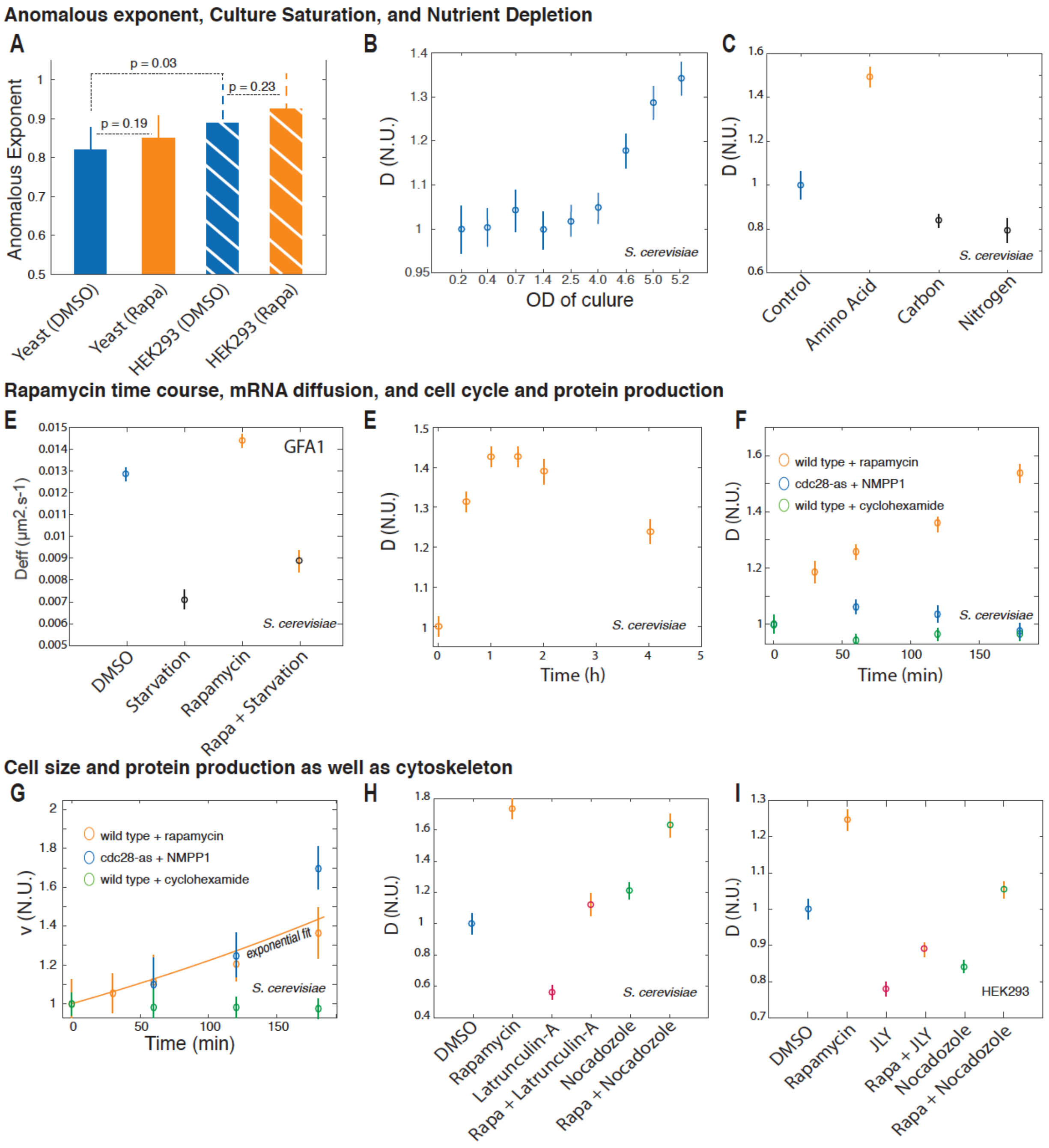

Figure S2: **Effects of culture conditions on diffusion, and time course of rapamycin treatment. Cell volume increase, translation, and cytoskeletal pertubations do not explain rapamycin-dependent effects on GEM behavior.**

Anomalous exponent smilar in rapamycin and DMSO treatment but different between HEK293 and yeast. Related to figures 2 (**A**) Anomalous diffusion exponents, a measure of subdiffusive motion, are similar between DMSO and Rapamycin treatment in yeast and mammalian cells according the a Student's T-test while the exponent is higher in mammalian cells than yeast, indicating that mammalian cells appear to be less subdiffusive(p=0.03). (**B**) Effect of culture saturation on diffusion coefficent of 40-nm GEMs in BY4741 cells(Normalized Units (N.U.)) (**C**) The effects of 2 hours of amino acid depletion, 30 minutes of carbon starvation and 30 minutes of nitrogen starvation on the diffusion coefficeint of 40-nm GEMs in BY4741 cells. (**D**) Effect of rapamycin treatment on the diffusion coefficent of 40-nm GEMs in BY4741 cells over 4 hours. (**E**) Combined effects of starvation and rapamcyin treatment on the diffusion coefficeint of the MS2 tagged GFA1 mRNA. (**F** and **G**) Change in normalized volume (**F**) and coefficient of diffusion (**G**) over time for rapamycin treatment (orange), inhibition of cell cycle in conditional mutant cdc28-as allele background with NMPP1 (blue) and cyclohexamide treatment (green). (**H** and **I**) Actin and microtubule perturbations alter the diffusion of 40-nm GEMs in yeast and mammalian cells but do not abolish the effect of rapamycin.

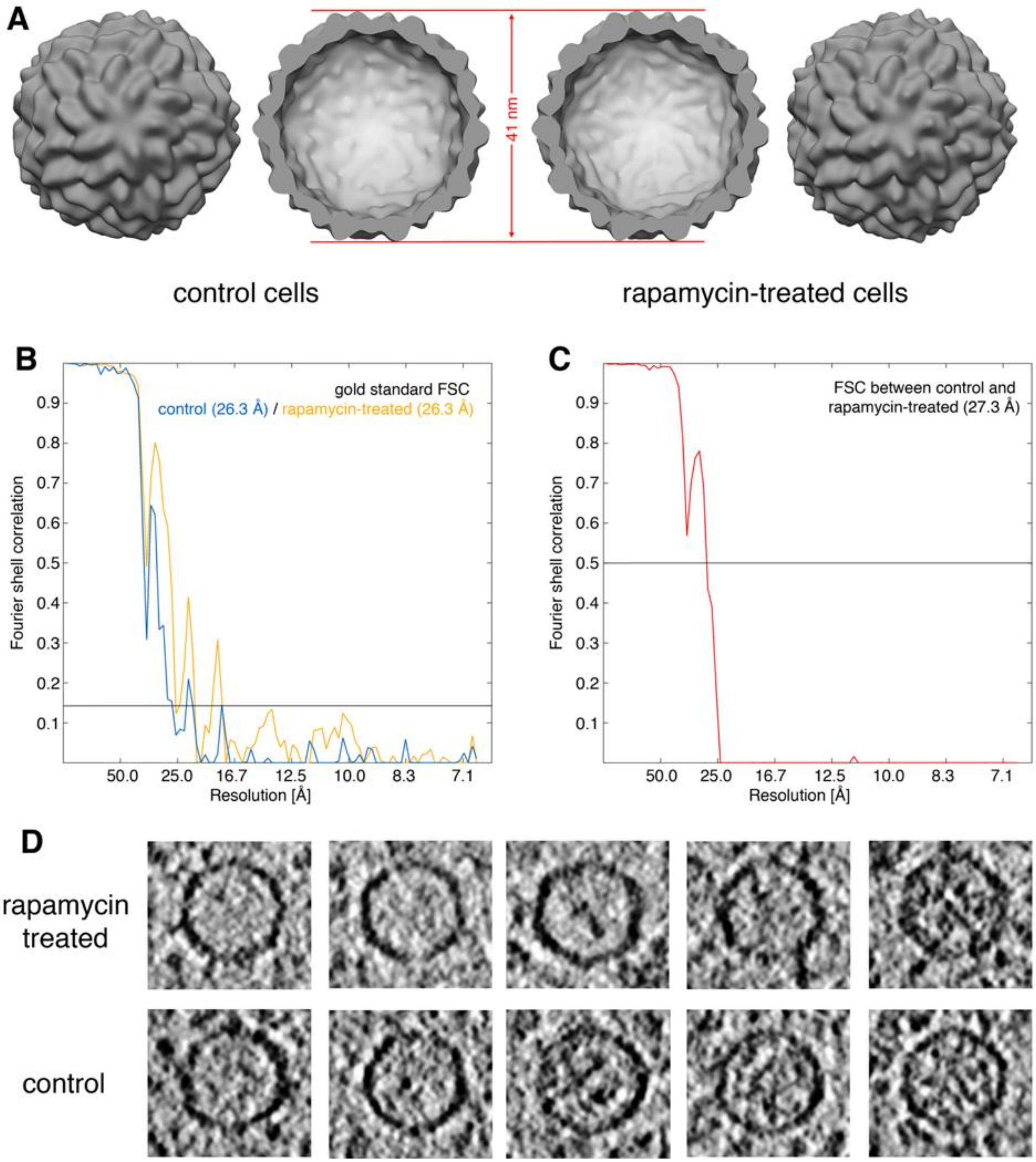

Figure S3: GEM structures from control and rapamycin-treated cells are indistinguishable. Related to figures 1 and 5. (**A**) GEM subtomogram averages obtained for control (left panels) and rapamycin treated (right panels) cells filtered to 26.3 Å resolution. In the central two panels, averages have been sliced open to show the interiors. (**B**) Fourier shell correlation (FSC) between subtomogram averages derived fro two independent halves of the data (gold standard) for control (blue) and rapamycin-treated (orange) cells. Resolution was determined to 26.3 Å in both cases using the FSC = 0.143 resolution criterion. (**C**) FSC between the two resolution-limited subtomogram averages obtained for control and rapamycin-treated cells. High correlation (FSC > 0.5) within the trustworthy resolution range suggests that GEM structures under both conditions are identical. (**D**) Gallery of individual GEM particles from control (lower row) and rapamycin-treated (upper row) cells. Each image corresponds to a central tomogram slice through the GEM particle. The amount of cargo within the GEM lumen varies.

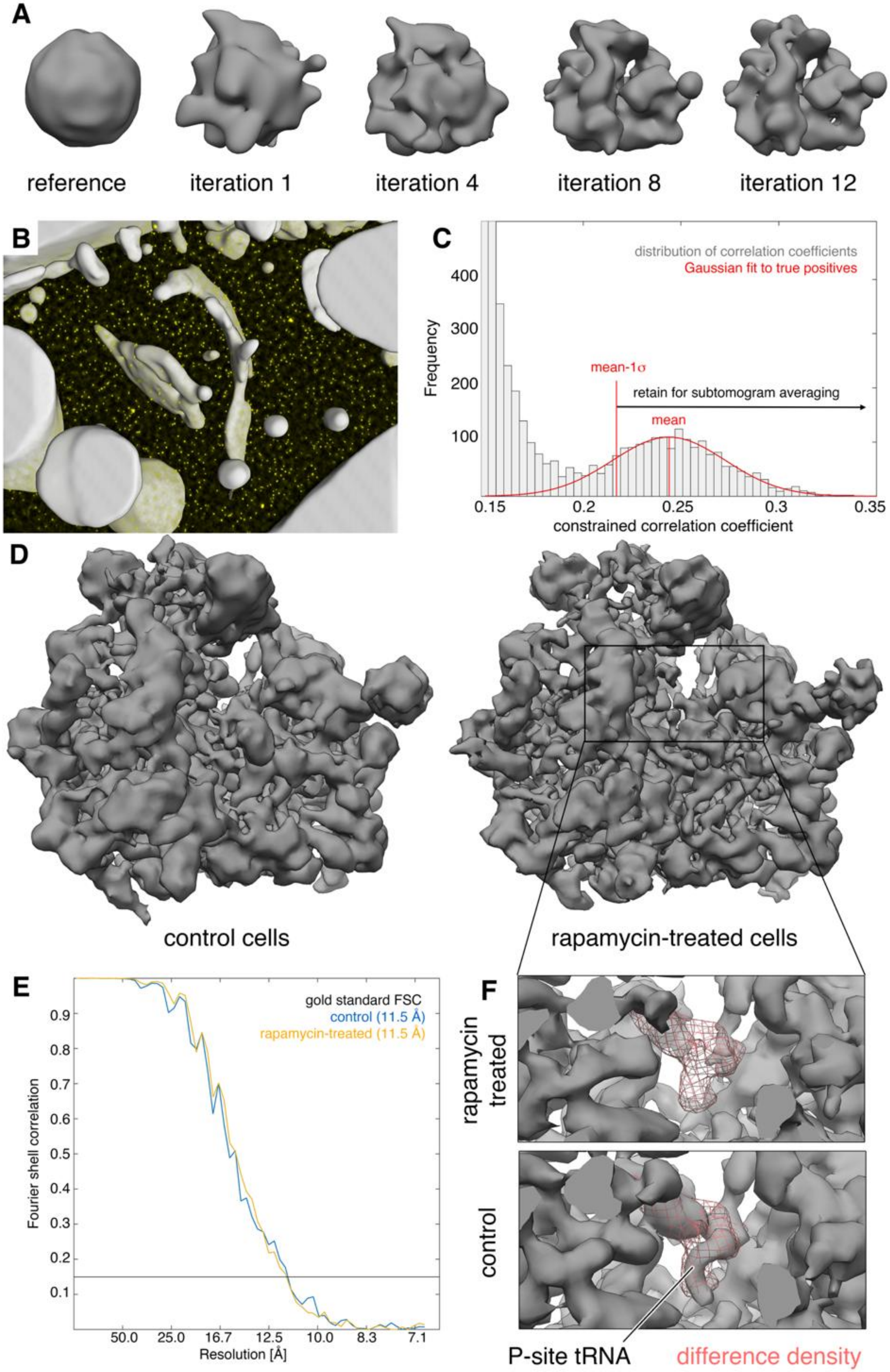
A
reference
iteration 1
iteration 4
iteration 8
iteration 12
B
C
distribution of correlation coefficients
Gaussian fit to true positives
Frequency
400
300
200
100
mean-1σ
retain for subtomogram averaging
mean
0.15
0.2
0.25
0.3
0.35
constrained correlation coefficient
D
control cells
rapamycin-treated cells
E
gold standard FSC
control (11.5 Å)
rapamycin-treated (11.5 Å)
Fourier shell correlation
0.9
0.8
0.7
0.6
0.5
0.4
0.3
0.2
0.1
50.0
25.0
16.7
12.5
10.0
8.3
7.1
Resolution [Å]
F
rapamycin treated
control
P-site tRNA
difference density

Figure S4: **Ribosomes can be located with single molecule precision via cryo-electron tomography and template matching. Related to figures 5 and 6. (A)** 500 manually selected ribosome-containing subtomograms were iteratively aligned with a sphere as a starting structure (left). Within 12 iterations, the averaged density converged to a yeast 80S ribosome (right) that was subsequently used as a purely data-driven *de novo* template for correlation-based ribosome localization (template matching) in the tomograms. **(B)** Example cross correlation function (yellow) obtained from template matching against the *de novo* ribosome structure, superposed with the non-cytosolic cellular volume (gray) excluded from the analysis. Peaks in the cross-correlation function (yellow spots) indicate putative ribosome positions. **(C)** Distribution of cross-correlation coefficients for the 5000 highest-scoring peaks, which were extracted from the cross-correlation volume depicted in B while imposing a minimal Euclidean distance of 18.9 nm (9 voxels) between peaks. A Gaussian function (red) was fit to the distribution of coefficients corresponding to true positives. The integral of the Gaussian function corresponds to the number of ribosomes included in the cytosolic volume. **(D)** Ribosome subtomogram averages obtained for control (left) and rapamycin-treated (right) cells filtered to 11.5 Å resolution. **(E)** FSC between subtomogram averages derived from two independent halves of the data (gold standard) for control (blue) and rapamycin- treated (orange) cells. Resolution was determined to 11.5 Å in both cases using the FSC=0.143 resolution criterion. **(F)** Enlarged view of the region indicated with a box in (D), comparing the ribosome structures from rapamycin-treated (upper panel) and control (lower panel) cells. The most significant density difference (red mesh, threshold level of 6 sigma) between both ribosome structures co-localizes with the P-site tRNA, which is resolved in the control but not the rapamycin-treated condition.

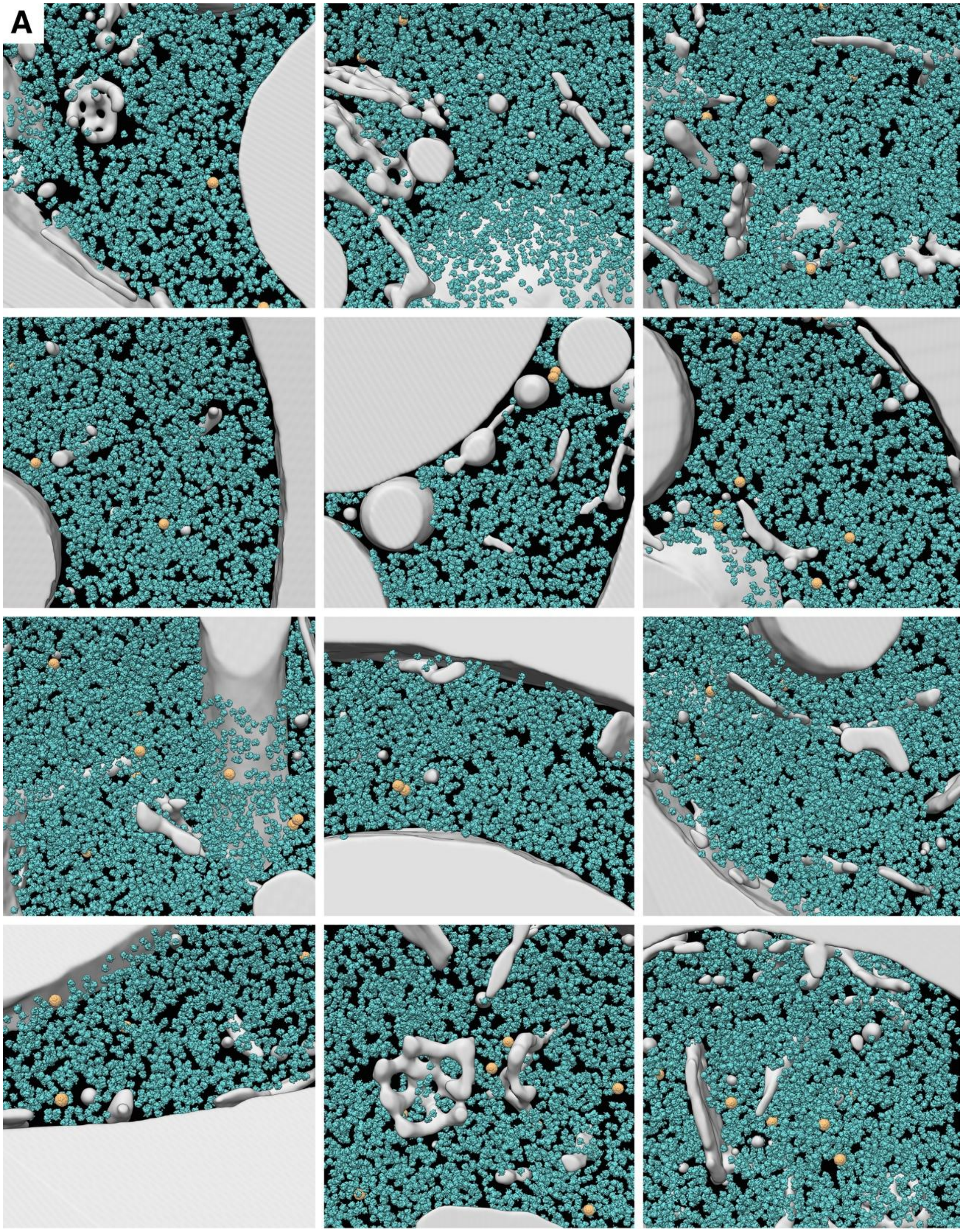
A

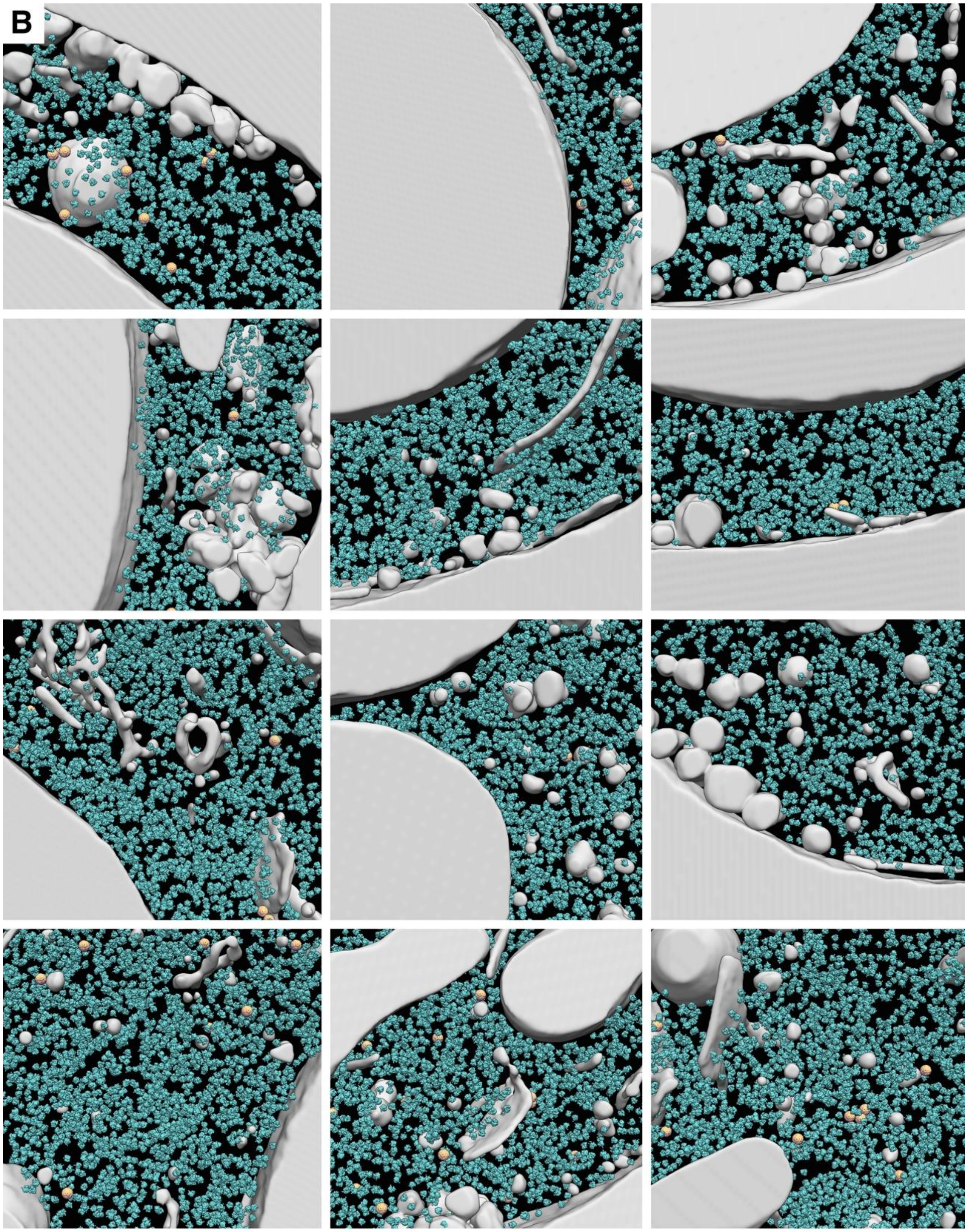
B

Figure S5: Gallery of 3D segmentations from the complete cryo-ET dataset. Related to figure 5. (A) Control yeast cells. **(B)** Rapamycin-treated yeast cells. Detected ribosomes are depicted in blue, GEMs in orange and the non-cytoplasmic volume that was excluded from the analysis in gray. The example tomograms from Fig. 5 and the 14th tomogram of control yeast cells are not pictured here.

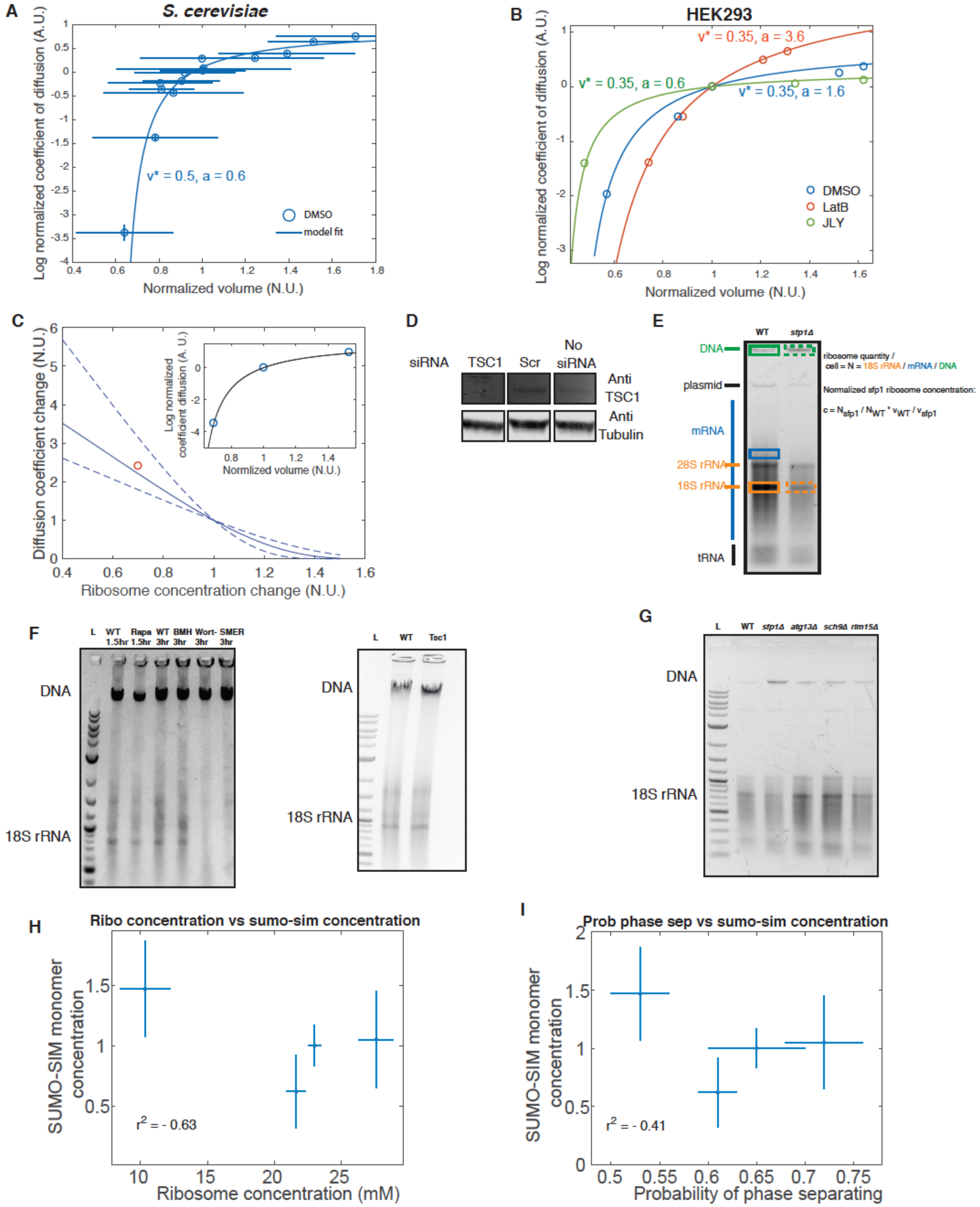
A
S. cerevisiae
Log normalized coefficient of diffusion (A.U.)
1
0.5
0
-0.5
-1
-1.5
-2
-2.5
-3
-3.5
-4
0.4
0.6
0.8
1
1.2
1.4
1.6
1.8
Normalized volume (N.U.)
v* = 0.5, a = 0.6
DMSO
model fit
B
HEK293
Log normalized coefficient of diffusion (A.U.)
v* = 0.35, a = 3.6
v* = 0.35, a = 0.6
v* = 0.35, a = 1.6
DMSO
LatB
JLY
1
0
-1
-2
-3
0.6
0.8
1
1.2
1.4
1.6
Normalized volume (N.U.)
C
Diffusion coefficient change (N.U.)
6
5
4
3
2
1
0
0.4
0.6
0.8
1
1.2
1.4
1.6
Ribosome concentration change (N.U.)
Log normalized coefficient diffusion (A. U.)
0
-2
-4
0.8
1
1.2
1.4
Normlized volume (N.U.)
D
siRNA
TSC1
Scr
No siRNA
Anti TSC1
Anti Tubulin
E
WT
sfp1Δ
DNA
plasmid
mRNA
28S rRNA
18S rRNA
tRNA
ribosome quantity / cell = N = 18S rRNA / mRNA / DNA
Normalized sfp1 ribosome concentration:
c = N_sfp1 / N_WT * v_WT / v_sfp1
F
L
WT 1.5hr
Rapa 1.5hr
WT 3hr
BMH 3hr
Wort- 3hr
SMER 3hr
DNA
18S rRNA
L
WT
Tsc1
DNA
18S rRNA
G
L
WT
sfp1Δ
atg13Δ
sch9Δ
rim15Δ
DNA
18S rRNA
H
Ribo concentration vs sumo-sim concentration
SUMO-SIM monomer concentration
1.5
1
0.5
r² = - 0.63
10
15
20
25
Ribosome concentration (mM)
I
Prob phase sep vs sumo-sim concentration
SUMO-SIM monomer concentration
2
1.5
1
0.5
0
r² = - 0.41
0.5
0.55
0.6
0.65
0.7
0.75
Probability of phase separating

Figure S6: **Validation of the Doolittle equation and determination of parameters using instantaneous volume change through osmotic stress, TSC western blot and 18S rRNA quantification, related to figures 4, 6 and 7.** (**A**) After performing hyper- and hypo-osmotic shocks to perturb cell volume and then immediately assessed the diffusion coefficient for 40nm-GEMs, we fitted the model (equation (S10) on *S. cerevisiae* and find that it is in very good agreement with our data, suggesting that the Doolittle equation reasonably describes the dependence of diffusion coefficient on volume fraction of crowding agent (r^2 = 0.85), and supplying parameters $\zeta : 0.6$, $\phi_0 / \phi_m : 0.5$. (**B**) We performed the same osmotic stress experiment to mammalian cells, and initially measured different parameters ($\zeta : 1.6$, $\phi_0 / \phi_m : 0.35$). Osmotic stress is known to strongly affect the actin cytoskeleton in mammalian cells, which was confirmed when we treated the cells with LatA at the same time we did the osmotic stress ($\zeta : 3.6$, $\phi_0 / \phi_m : 0.35$): the ζ interaction parameter of the GEMs with the environment increased. When the actin cytoskeleton was stabilized with JLY cocktail, we found that the 2 parameters of the model were closer to the yeast values: $\zeta : 0.6$, is very similar to yeast, suggesting that the interactions of the GEMs with the microenvironment is the same, and $\phi_0 / \phi_m : 0.35$ is lower, suggesting that mammalian cells are less crowded.(**C**) The non-osmotic volume and the ζ parameter for cells containing mRNP (inset) were calibrated in order to predict, for this type of particle, how the change in diffusion coefficient would be affected by a change in ribosome concentration, occurring through a rapamycin treatment. (**D**) TSC1 was targeted using Silencer Select siRNA (Thermo Fisher). Knockdown was validated by western blot using Hamartin/TSC1 with a tubulin control using standard techniques (see methods). (**E**) We extracted total nucleic acid by neutral phenol (see methods) and run the extract in a agarose gel, for the various chemical of genetic conditions explored. The gel is decomposed in the DNA band, that is used as a proxy for the amount of cells extracted, mRNA, rRNA and tRNA. To assess the relative amount of rRNA, as a proxy for ribosome amount, we normalized the band of rRNA to mRNA, and subsequently to DNA to get this quantity per cell. This number was extracted for each conditions, and normalized to the control: this gives us the relative change in ribosome number in HEK293 drug and siRNA treatments (**F**) and yeast mutants (**G**). (**H**) Sumo(10)-SIM(6) concentration (measured by flow cytometry) as a function of ribosome concentration (measured by DNA gel) (r^2=0.63). (**I**) Sumo(10)-SIM(6) concentration (measured by flow cytometry) versus probability of seeing phase separation in the crowding mutants (r^2=0.41).

STAR Methods

Contact for reagent and resource sharing

Requests for materials should be addressed to the Lead Contact, Liam Holt (liam.holt@nyumc.org)

Experimental Model and Subject Details

Yeast

BY4741 and W303 strains were used in this study as indicated in table S2. Exponentially growing cultures O.D. $\geq$ 0.1 and $\leq$ 0.4 were used in all experiments unless otherwise noted. Note: It is extremely important to avoid culture saturation - all cultures were started from single colonies and grown overnight to log phase (typically we set up 1/5 serial dilutions to catch one culture at the correct OD). If cultures saturate, it takes many generations to reset the cellular rheology. All strains were grown at 30^{o} C in a rotating incubator.

HEK293 Cells

Mammalian cells were maintained at 37^{o} C with 5% CO_2. HEK293 and HEK293T were grown in high glucose DMEM (Life Technologies) supplemented with 10% fetal bovine serum (FBS; Gemini Bio-products), penicillin (50 U ml^{-1}) and streptomycin (0.05mg.ml^{-1}) (Life Technologies) unless otherwise stated.

Plasmid construction

The open reading frames encoding the *Pyrococcus furious* encapsulin and *Aquifex aeolicus* (AqLS) lumazine synthase protein based on the published crystal structures (www.rcsb.org 2E0Z and 1NQU respectively) were codon optimized for yeast and mammalian expression and synthesized as IDT gene blocks (www.idtdna.com). The

40nm-GEM plasmid for yeast expression was constructed by fusion at the 5' end of the gene with the yeast INO4 promoter and at the 3' (via a Gly-Ser linker) with the T-Sapphire fluorophore (Zapata-Hommer and Griesbeck, 2003) by Gibson assembly into the pRS305 vector (pLH0497: pRS305-PINO4-PfV-GS-Sapphire). The Mammalian expression vector was assembled similarly into the pCDNA3.1 vector (Thermo Fisher) with the CMV2 promoter (pLH611: pCDNA3.1-CMVP2-PfV-GS-Sapphire-GGS). To make a Lentiviral vector (pLH1337: CMV-PfV-Sapphire-IRES-DsRed-WPRE) to express 40nm-GEMs, the PfV-GS-Sapphire sequence was digested from pLH611 and incorporated into a Clontec V4 vector via Gibson assembly. We empirically determined that Sapphire was brighter than GFP in the context of GEMs, presumably because the long Stokes-shift of this fluorophore avoids some of the autoquenching that may occur on the crowded surface of these particles. However, this crowded environment also appears to affect the photochemistry of Sapphire such that fluorophore excitation is efficient at 488 nm – thus, for imaging purposes, we used settings optimized for GFP (see Imaging below). The 20nm-GEM for yeast expression was assembled by fusion at the 5' with the yeast HIS3 promoter and at the 3' (via a Gly-Ser linker) with the T-Sapphire fluorophore by Gibson assembly into the pRS306 vector (pLH1144:pRS306-PHIS3-AqLumSynth-Sapphire). μNS-GFP (PHIS3-GFP-μNS-URA3) particles were constructed by Gibson assembly of the published N-terminal GFP fusion to the C-terminal fragment of μNS (residues 471-721) (Broering et al., 2005) together with the yeast HIS3 promoter into the pRS306 vector (pLH1125: pRS306-PHIS3-GFP-muNS). The Sumo(10)-Sim(6) yeast reporter(pLH1388:pAV106-pTDH3-mCherry-10xSumo-6xSIM) plasmid was generated by chemical synthesis of mCherry fused to a linked

Sumo(10)-Sim(6) sequence that was based on the human sequence and then codon optimized for yeast. The mammalian Sumo(10)-Sim(6) was graciously gifted from the lab of Mike Rosen. All yeast plasmids were integrated into the host genome.

Yeast transformation

Yeast strains were created by transforming with a LiAc based approach according to standard methods. BY4741 deletion mutants were obtained from the Yeast Deletion Collection. pLH0497:pRS305-LEU2-PINO4-PfV-GS-Sapphire or pRS306-URA3-PHIS3-PfV-GS-Sapphire was transformed into the collection to allow for screening of mutants or into BY4741 and W303 strains for the rest of the experiments. The cdc28-as1 strain was taken from (Bishop et al., 2000). A list of yeast strains constructed is provided in Table S2 and STAR Key Resources Table.

Virus production and cell transduction

In order to create lentivirus, 800,000 HEK293T cells were plated in 10mL media in 15cm dishes. The next day, each well was transfected with 24 μg vector, 1.2 μg tat, 1,2 μg rev, 1,2 μg gag/pol, and 2.4 μg of vsv-g DNA with 90 μL trans-IT in 2mL DMEM. Supernatants were collected at 24, 48, and 72 hours after transfection and stored at 4 ^{o}C until they were spun at 16.5K for 90 minutes on a Beckman L-80 Ultracentrifuge. Viral pellets were resuspended in 1/50th of their original volume in DMEM (with 10% FBS) and stored at -80 ^{o}C until their use. Stable HEK293 cell lines were created by transfection with (pLH611: pCDNA3.1-CMVP2-PfV-GS-Sapphire-GGS) followed by neomycin selection. Additional HEK293 cell lines were created by lentiviral transduction with pLH1337-CMV-PfV-Sapphire-IRES-DsRed-WPRE. No differences in terms of cellular rheology were seen between these different methods. In order to transduce these cell lines, 50,000 cells were plated in 2mL of media in 6 well plates. The next day, media was removed and replaced with media containing 8 μg/mL polybrene. Between 1-20 μL of concentrated virus was added to the well and then the media was replaced after 24 hours.

Method Details

Drug treatments

In order to inhibit mTORC1 signaling, we treated with rapamycin (Tocris Bioscience, Avonmouth, Bristol, UK) at 1 μM for 2 hours in yeast and 3 hours in mammalian cells. To block translation we added 1 μM cycloheximide (Sigma-Aldrich, Allentown PA). In order to block ribosome production in HEK293 cells, we treated with PolI inhibitors BMH21 and CX5461 (Selleckchem, Houston, Texas, USA) at concentrations of 10uM and 500nM, respectively for 3 hours. In order to increase autophagy in HEK293 cells, we treated with SMER28 (Tocris Bioscience, Avonmouth, Bristol, UK) at a concentration of 5uM for 3 hours. In order to decrease autophagy in HEK293 cells, we treated with 800nM Wortmannin (Cell Signaling Technology, Danvers, MA, USA) for 2 hours. In order to de-polymerize actin and microtubules in yeast we incubated the cells with 200 μM latrunculinA and 50 μM nocodazole (Tocris) for 30 minutes. In order to depolymerize actin in HEK293 cells, we treated with 10μM latrunculin A (tocris) for 20 minutes. In order to freeze the actin cytoskeleton, we treated with 10μM y27632 (selleckchem) for 10 minutes then added jasplakinolide (Cayman) and latrunculinB (Tocris) to final concentrations of 8μM jasplakinolide and 5μM latrunculinB and imaged immediately after. (Peng et al., 2011). All stocks were prepared in DMSO and stored at -20 ^{o} C until needed. DMSO was used as an vehicle control in all experiments.

Imaging and direct particle tracking

Single particle tracking in *Saccharomyces cerevisiae* was performed for the 20nm-GEMs, 40nm-GEMs, AqLS particles, GFA1 mRNA particles, and μNS. The particles were imaged using TIRF Nikon TI Eclipse microscope at 488nm, and their fluorescence was recorded with a scMOS (Zyla, Andor) with a 100x objective (pixel size 0.093 μm), with a time step that depends on the particles. The GEMs were imaged at a rate of one image every 10ms, whereas both the RNA particles and the μNS were imaged at 100ms time step.

Single particle tracking in HEK293 cells was performed for 40nm GEMs using an Andor Yokogawa CSU-X confocal spinning disc on a Nikon TI Eclipse microscope and their fluorescence was recorded with a sCMOS Prime95B camera (Photometrics) with a 100x objective (pixel size 0.11 μm), at 10ms image capture rate.

The tracking of particles was realized through the Mosaic suite of FIJI, using the following typical parameters: radius $=3$, cutoff = 0, 10 $\%$ of intensity of fluorescence, a link range of 1, and a maximum displacement of 8 px, assuming Brownian dynamics.

Extraction of the rheological parameters

Various parameters were extracted from the trajectories of particles. For every trajectory, we calculated the time-averaged mean-square displacement (MSD), as defined in (Munder et al., 2016a) as well as the ensemble-average of the time-averaged MSD. As observed in the insets figure 2D and 2E, where the ensemble-averaged MSD is plotted as a function of time in a log-log plot, the diffusion of the tracer particle is subdiffusive, and generally obeys the following law:

$$\mathrm{MSD}(\tau) = 4K\tau^{\alpha} \tag{1}$$

where α is the power exponent of the anomalous diffusion, $\alpha \leq 1$ in the case of a subdiffusive behavior. In this case, the apparent diffusion coefficient, K, is not in units of $\mu\mathrm{m}^2$/s, but rather in units of $\mu\mathrm{m}^2/\mathrm{s}^{\alpha}$.

To characterize individual particle trajectories, we simplified to a linear MSD fit to measure an effective diffusion at short time scales (less than 100 ms for GEMs, 1s for mRNP and μNS particles). To do this, we calculated the MSD and truncated it to the first 10 points, and fitted it with the following linear relationship:

$$\mathrm{MSD}_{\mathrm{truncated}}(\tau) = 4D_{\mathrm{eff}}\tau \tag{2}$$

where D_{eff} is the effective coefficient of diffusion of the tracer particle, and plotted the distribution of this effective diffusion coefficient. We use the Kolmogorov-Smirnov statistical test to assess the statistical difference between distributions (kstest2 function in Matlab).

Culture Saturation and nutrient depletion experiments

Culture O.D. was measured from 0.2 to 5.2 O.D. on a Thermo Scientific Nano-Drop One spectrophotometer followed by GEM tracking as previously described. To measure the effects of depletion of Amino Acids, Carbon and Nitrogen, synthetic complete media was prepared without 20g/L Dextrose (carbon starvation), without Drop-put mix complete w/o Yeast Nitrogen Base (US Biological), or without Yeast Nitrogen Base w/o

Amino acids (Difco). Since Dextrose is the major source of osmolytes in SCD media, 18g/L of sorbitol was added to restore regular osmolarity in the carbon starvation condition. In order to ensure that any dextrose-containing media was removed, cells were spun down once at 3000 RPM then resuspended in starvation media. After plating on ConA treated imaging dishes the cells were then washed 4 times in fresh starvation media.

mTORC1 overexpression - TSC1 siRNA experiments

TSC1 (s14433 or s14434) was targeted by Silencer Select siRNAs from Thermo Fisher Scientific. 75 pmoles of siRNA were transfected using Lipofectamine RNAiMAX transfection reagent from Thermo Fisher Scientific as per manufacturer's instructions. Cells containing GEMs were assayed for diffusion at 72 hours post transfection. Knockdown was validated by western blot using Hamartin (TSC1) (D43E2) Rabbit mAb #6935 from Cell Signaling Technologies using standard techniques.

40-nm and 20-nm GEM purifcation for negative stain EM

Purification was performed at 4°C, unless otherwise noted. Two liters of of yeast cells were grown overnight then lysed by cryogenic lysis in buffer B1 (20 mM Tris–HCl (pH 7.5), 10 mM MgCl2, 50 mM NH4Cl, 10 mM 2-mercapthoethanol, 10% glycerol (v/v), 1 mM PMSF, 2 mM spermidine). Cell debris removed by centrifugation at 9200g for 25 min. Next the lysate was warmed to 55°C for 30 min. The supernatant was further clarified by centrifugation at 38,900g for 1 h. The partially purified 40-nm GEM or 20-nm GEM particles were pelleted by ultracentrifugation at 185,000g for 3 h and then the particles were resuspended in buffer B1 (20 mM Tris–HCl (pH 7.5), 10 mM MgCl2, 50 mM NH4Cl, 10 mM 2-mercapthoethanol, 10% glycerol (v/v), 1 mM PMSF, 2 mM spermidine). This suspension was gently mixed with 20% Triton X-100 in KCl buffer (20 mM Tris–HCl (pH 7.5), 10 mM MgCl2, 50 mM NH4Cl, 10 mM 2-mercapthoethanol, 10% glycerol (v/v), 1 mM PMSF, 2 mM spermidine, 2.5 M KCl) at 30°C. Then the suspension of 40-nm GEM or 20-nm GEM particles was carefully placed on a cushion of 20% sucrose in buffer B1 and pelleted by ultracentrifugation at 185,000g for 20 h. Next, the particles were resuspended in buffer B2 (20 mM Tris–HCl (pH 7.5), 5 mM MgCl2, 50 mM NH4Cl, 10 mM 2-mercapthoethanol, 10% glycerol (v/v), 1 mM PMSF, 2 mM spermidine) and then gently mixed with buffer C (20 mM Tris–HCl (pH 7.5), 5 mM MgCl2, 50 mM NH4Cl, 10 mM 2-mercapthoethanol, 10% glycerol (v/v), 1 mM PMSF, 1.5 M KCl, 2 mM puromycin, 2 mM guanosine triphosphate) at 30°C. Finally, the particles were placed carefully on a cushion of 25% glycerol in buffer B2 and pelleted by ultracentrifugation at 185,000g for 15 h.

Negative stain transmission electron microscopy

Purified proteins are put on carbon coated 400 mesh copper/rhodium grids (Ted Pella Inc., Redding, CA), stained with 1% aqueous uranyl acetate, examined under Philips CM-12 electron microscope and photographed with a Gatan (4k x2.7k) digital camera.

Cryo-EM grid preparation and data acquisition

W303 *S. cerevisiae* were grown on YPD plates for two days, then suspended in SCD media at low cell concentration by serial dilution and grown overnight at 30^{o} C on a roller drum to an OD of 0.25. Cells were then incubated with 1 μM rapamycin in DMSO or only DMSO (control) for 2 h until an OD of 0.55. Cells were frozen onto EM grids from 2-2.5 h after addition of the drug. 4 μL of culture was applied to R2/1 holey carbon copper EM grids (Quantifoil) and immediately vitrified by plunge-freezing into a liquid ethane/propane mixture with a Vitrobot Mark IV (FEI, The Netherlands) using a blot time of 10 s, a blot force of 10, and a chamber conditioned to 25 °C and 90% humidity. EM grids with vitrified yeast cells were transferred either to a Quanta or Scios dual-beam microscope (both FEI, The Netherlands) for focused ion beam micromachining. The vitrified cells were platinum coated with organometallic platinum and subsequently thinned by scanning gallium ions in a stepwise fashion from both sides. This yielded vitrified cellular sections of 100-200 nm thickness that were suitable for cryo-electron tomography (Schaffer et al., 2017). EM grids with milled samples were transferred to a Titan Krios TEM (FEI, The Netherlands) operated at an acceleration voltage of 300 kV, an object pixel size of 3.42 Å and a nominal defocus of -6 μm. The TEM was equipped with a Quantum energy filter (Gatan) and a K2 summit direct electron detector (Gatan) operated in movie mode (12 frames per second). Single-axis tilt series were acquired in SerialEM (Mastronarde, 2005) using a bi-directional tilt scheme covering a tilting range of approximately -60° to 60° with a 2° angular increment. Depending on the pre-tilt of cellular sections in the TEM, the two tomogram halves were connected at either +20° or -20° tilt. The cumulative electron dose for a tilt series was 70-120 electrons per Å2, depending on the sample thickness.

Tomogram reconstruction

Frames from the K2 direct detector were aligned with MotionCor2 (Zheng et al., 2017) using 3x3 patches for local alignment. For each tilt series, the resulting frame-aligned projections were sorted according to their tilt angles and compiled into an image stack that was loaded into IMOD for tilt series alignment via patch tracking. Projection-wise translations and rotations determined during patch tracking were extracted from IMOD's output files and used for tilt series alignment in TOM/AV3 (Förster and Hegerl, 2007; Nickell et al., 2005). Phase reversals introduced by the contrast transfer function (CTF) were determined on each individual projection using strip-based periodogram averaging (Eibauer et al., 2012) in TOM/AV3 and corrected in PyTom (Hrabe et al., 2012). Finally, the aligned CTF-corrected tilt series was weighted for subsequent reconstruction of tomographic volumes via weighted back projection (AV3/TOM). For reconstruction of binned tomograms, the tilt series was scaled to 2.1 nm in Fourier space (AV3/TOM).

Determination of the cytosolic volume in tomograms

Binary masks encompassing exclusively the cytosolic volume were generated by manual segmentation of tomograms in Amira (FEI, The Netherlands). As each voxel corresponds to a volume of $(2.1\ \text{nm})^3 = 9.26\ \text{nm}^3$, the exact cytosolic volume included within the tomogram could be obtained by counting the voxels encompassed by the mask.

Subtomogram analysis

A) Ribosome: To generate a data-driven *de novo* template for correlation-based ribosome localization, 500 ribosomes were manually selected from one of the tomograms and reconstructed as described below. The subtomograms were iteratively aligned using fast rotational matching (FRM) (Chen et al., 2013) implemented in PyTom with a featureless sphere as a starting reference (Figure S4A). The average converged into a ribosome within 12 iterations and was subsequently used as a template for correlation based localization of ribosomes (Frangakis et al., 2002) in all tomograms.

For each tomogram, the cross-correlation function resulting from template matching was masked to include only the cytosolic volume of the cell (Figure S4B) and the 5000 highest-scoring peaks were extracted. To avoid multiple detection events for the same ribosome, a minimal Euclidean distance of 18.9 nm (9 voxels) between peaks was imposed. The distribution of correlation coefficients for the extracted peaks showed clear separation of coefficients corresponding to true and false positives (Figure S4). This allowed fitting of a Gaussian function to the distribution of coefficients corresponding to true positives and thus quantification of ribosome abundance within the cytosolic volume.

For detailed analysis of ribosome structures, all ribosomal particles with correlation coefficients better than one standard deviation below the mean of the fitted Gaussian function were retained and reconstructed at full spatial resolution in PyTom from the CTF-corrected, weighted and aligned projections covering approximately the first half of the tilt series. Projections corresponding to the second half of the tilt series were excluded at this step due to excessive beam damage that dampens high-resolution signal. The reconstructed subtomograms were aligned until convergence with Relion's gold standard "3D auto-refine" functionality, which is now available for subtomograms (Bharat et al., 2015). During subtomogram averaging, Relion's 3D CTF model was used to compensate for beam damage with the recommended B-factor of -4 per electron per $Å^2$. Resolution of the resulting averages was estimated based on Fourier shell cross-correlation (FSC) of two completely independent halves of the data using FSC = 0.143 as the cutoff criterion. For computation of the difference density between ribosome structures from control and rapamycin-treated cells, the averages were filtered to 15 Å resolution, normalized according to density mean and density standard deviation, and subtracted from each other. The UCSF Chimera software package (Goddard et al., 2007) was used for visualization of EM densities.

B) GEMs: GEMs are readily visible in tomograms as high-contrast sphere-like particles (Figure S4D). Consequently, template matching against a hollow sphere of appropriate size in combination with visual inspection of the 50 highest scoring cross-correlation peaks in the cytosolic volume allowed highly specific localization of GEMs in the tomograms. Subtomogram reconstruction, alignment and resolution estimation were performed as described for the ribosome, with the only exception that icosahedral symmetry was applied during subtomogram alignment.

FCS and coefficient of diffusion of 2xGFP

A custom-modified inverted microscope (Nikon Eclipse Ti; Nikon Instruments) was used for FCS measurements. Prior to each measurement, a focus spot within a cell was located by eGFP epifluorescence. A 100-ps pulsed 482 nm diode laser (PicoQuant) was coupled to a single-mode fiber and collimated to a 4-mm diameter, then focused on the sample through a 100x objective (CFI Apo 100x Oil immersion TIRF NA 1.49; Nikon Instruments), with the laser power of 0.2 μW before the objective. The focus spot was calibrated with a fluorescent dye with a known diffusion coefficient (Alexa 488, D = 435 μm^2/s (Petrášek and Schwille, 2008)). Each FCS measurement was the average of 10-20 cells. Fluorescence emitted from the sample was passed through a 50-μm pinhole (Thorlabs), and focused to a bandpass-filtered single-photon avalanche diode with a 150 x 150 μm element (PDM module; Optoelectronic Components). The resulting fluorescence fluctuation was processed by a hardware correlator (Correlator.com), which generated the autocorrelation function. See table S1 for results and more details on the fitting procedure of the autocorrelation function.

Fluorescence Correlation Spectroscopy Calculations

FCS data were fitted using a "blinking and anomalous diffusion" model, that has the following form (Brazda et al., 2011):

$$G(\tau)=\frac{1-F+Fe^{-\tau/t_f}}{1-F}\frac{1}{N}\left(1+\left(\frac{\tau}{t_d}\right)^{a}\right)^{-1}\left(1+\frac{1}{s^2}\left(\frac{\tau}{t_d}\right)^{a}\right)^{-2} \tag{4}$$

The term on the left before the $1/N$ is the blinking term corresponding to the properties of GFP. In this term, t_f was measured independently from whole cell lysate, $t_f = 3.5\text{x}10^{-5}$ s. The term on the right corresponds to the anomalous 3D diffusion of GFP, where t_d is the particle residence time in the focus volume, $t_d = w^2/4D$. $w = 220nm$ and s/w are the radial and axial dimensions of the 3D Gaussian laser focus, respectively, and they were measured using a dye with a known diffusion coefficient (Alexa Fluor 488). In practical terms, s does not affect the fit, and was fixed to be $s = 10$. The result of the fit is summarized in table 1, and yields $D_{\text{DMSO}} = 13.3 \pm 1.3 \mu m^2/s$ and $D_{\text{rapamycin}} = 12.2 \pm 2.8 \mu m^2/s$, which are not significantly different (3 biological replicates, n ≥ 10 cells per condition). Note that the anomalous diffusion exponent a is in both cases : 0.8, close to the measured anomalous parameter measured for GEMs. We chose an anomalous model, as commonly used in the literature to describe motion of GFP in a cell (Slaughter et al., 2007), and as it yielded a better fit than the normal diffusion model.

Parameter	DMSO condition	Rapamycin condition
N	1.22 ± 0.03	1.49 ± 0.09
F	0.16 ± 0	0.29 ± 0.05
t_f (s)	$3.5\text{x}10^{-5}$ (fixed)	$3.5\text{x}10^{-5}$ (fixed)
t_d (s)	$(9.1 \pm 0.9) \cdot 10^{-4}$	$(9.9 \pm 2.3) \cdot 10^{-4}$
s	10 (fixed)	10 (fixed)
a	0.79 ± 0.05	0.77 ± 0.07

Table S1: Results of fitting the blinking anomalous diffusion model to FCS data.

Osmotic perturbation experiments and cell volume measurement

In order to calculate the dependence of the volume fraction of crowding agent on diffusion of GEMs, we performed hyper- and hypo-osmotic stresses (see model below). LH2129 (BY4741 + PINO4::PINO4-PfV-GS-Sapphire-LEU2) cells were grown in log phase to an OD of 0.3, then spun down for 1 minute at 10000 rpm. Cells were washed with fresh medium, and placed in synthetic complete with dextrose medium complemented with 0M, 0.5M, 1M, 1.5M or 2M of sorbitol. A subset of cells were directly (within 15 minutes) imaged for diffusion, and phase pictures were taken in order to assess cell area as a proxy for cell volume. The rest of the cells were left at various ODs in a shaker at 30^o C to adapt to the osmotic stress and grow overnight. The next day, cells were imaged for diffusion and cell volume (green points (Figure 8), to check that cell volume and the diffusion of particles had recovered to their nominal values. These pre-adapted cells (which have built up a high concentration of internal osmolyte) were then spun down and placed in regular CSM, creating a hypo-osmotic stress of -0.5M, -1M, -1.5M and -2M, and immediately imaged for diffusion and cell volume. The same process was used for HEK293 cells, with osmotic stress of 0.25M and 0.5M sorbitol. Cells were trypsinized and their volume measured from their area when the cells were spherical.

SUMO-SIM protein purification

Proteins were expressed in Rosetta2 DE3 competent cells by induction with 100 μM IPTG for 18 hr at 16°C. 4 liters of bacterial culture were collected and centrifuged at 4000rpm for 20 min at 4°C. The cell pellet was resuspended in 100 ml cold lysis buffer (50mM NaH2PO4, 300mM NaCl, 10 mM imidazole pH7.6) containing 1 mM PMSF. After sonication, the lysate was centrifuged at 12000rpm for 30 min at 4°C. The supernatant was mixed with 8 ml of 50％ slurry of Ni-NTA beads (Qiagen). The lysate was incubated with beads for 2 hour at 4°C. The bound beads were collected by centrifugation at 500g for 1 minute and rinsed 3 × with 30 ml bacterial wash buffer containing (50mM NaH2PO4, 300mM NaCl, 20 mM imidazole pH7.6). The bound proteins were eluted with 8ml elution buffer (50mM NaH2PO4, 300mM NaCl, 500 mM imidazole pH7.6).

The elution was exchanged into 2 ml of SUMO-SIM protein buffer (150mM KCl/20mM HEPES pH7/1mM MgCl2/1mM EGTA/1mM DTT) using a PD10 column (GE Healthcare), followed by further concentrating to 300-600 μM with Amicon Ultra 30K device (Millipore) at 4°C.

SIM is tagged with Alexa Fluor® 488, not fused with GFP. The protein was conjugated with Alexa Fluor® 488 with large scale antibody/protein labeling Kits (A10235, Thermo Scientific).

In vitro phase separation experiment

In order to determine if ribosomes are capable of acting as a crowding agent *in vitro*, we added purified ribosomes from an *in vitro* translation kit (IVT) (NEB, Ipswich, MA) to a mix of purified Small Ubiquitin like Modifier (SUMO) 60 μM module and SUMO Interaction Motif-GFP (SIM-Alexa Fluor 488) 60 μM module. Ribosomes were added at the same concentrations measured *in vivo* by cryo-ET as well as at an intermediate concentration. Ribosomes, SUMO, and SIM were mixed in a well of a 384 well imaging plate, the top was then covered with clear tape and then the plate was allowed to sit overnight in order to reach a steady-state before imaging. The plate was imaged on an Andor Yokogawa CSU-X confocal spinning disc on a Nikon TI Eclipse microscope and GFP fluorescence was recorded with an scMOS (Zyla, Andor) camera with a 100x objective (pixel size 0.1 μm). Images were loaded in FIJI and the partition coefficient (amount of protein that has condensed into liquid droplets versus protein dissolved in the bulk aqueous phase) was calculated by segmenting the image into two categories: bright droplets and background. Then the total amount of fluorescent protein was measured in each category through using the raw integrated density value. The partition coefficient was taken as the ratio of protein in the condensed phase versus the bulk phase and plotted in MATLAB.

In vivo phase separation experiments

In order to determine the effects of changes of ribosome concentration via mTORC1 signaling on phase separation, we expressed a mCherry-SUMO(10)-SIM(6) fusion protein in yeast (pLH1392) and mammalian cells (pLH 1393). WT and mutant yeast cells were grown overnight to log phase and then treated with rapamycin for 2 hours. Sorbitol was added in the last ten minutes in indicated conditions. Mammalian cells were treated for 3 hours with rapamycin with sorbitol added in the final 30 minutes where indicated. TIRF microscopy on a Nikon-TI microscope was performed using a 561 nm laser sample through a 100x objective (CFI Apo 100x Oil immersion TIRF NA 1.49; Nikon Instruments). Images were segmented in FIJI to determine the 1) average size of droplets, 2) number of droplets and 3) number of cells. In the actute rapamycin / sobitol treatment conditions we then used these data to define the total phase separated area as:

$$\frac{avg\ size * number\ of\ droplets}{number\ of\ cells} \tag{3}$$

Next, we expressed the mCherry-SUMO(10)-SIM(6) fusion protein in the ribosome biogenesis/autophagy mutants shown to have an effect on crowding. We reasoned that these mutants would be a better test of our hypothesis as they do not suffer the acute effects of rapamycin but rather sit at steady state. In these mutants we measured the likelihood of having a droplet of any size and related it to crowding and protein concentration by flow.

SUMO-SIM protein concentration and yeast cell size

Cells were grown to log phase between O.D. 0.1 and 0.4 and then analyzed on a SONY SH800 Cell Sorter. Fluorescence was recorded for the mCherry-tagged SUMO(10)-

SIM(6) fusion protein for every cell and then the average fluorescence intensity was extracted using Flow-Jo. These values were normalized to WT and then averaged across replicates.

Quantification and Statistical Analysis

Distributions of effective diffusion coefficients were compared using the Kolmogorov-Smirnov test in Matlab using the kstest2 function. Comparison of anomalous exponenents between and within yeast and mammalian treatments was conducted using a student’s t-test.

Crowding regulation through control of ribosome concentration.

Model Basis

In the following, we derive a model of crowding control in the cell. The purpose of the model is to link cell volume change to changes in the diffusion of a tracer particle, like our 40nm-GEMs. We assume that there is a major source of crowding within the cell, that is impacting the diffusion coefficient of 40nm-GEMs. We express the diffusion of the tracer particle as a function of volume fraction of the major crowder source, ϕ, using the phenomenological Doolittle equation (Doolittle, 1952):

$$D = D_0 e^{-\zeta/\Phi} = D_0 e^{-\zeta\varphi/(\varphi_m - \varphi)} \tag{5}$$

where D_0 is the coefficient of diffusion in an infinitely diluted solution, ϕ_m the maximum fraction of the crowder, and ζ is a constant. We write the volume fraction for the major source of crowder as:

$$\varphi = \frac{v_{\text{crowder}}}{v_{\text{water}} + v_{\text{crowder}} + v_{\text{other}}} = \frac{v_{\text{crowder}}}{v} \tag{6}$$

where v_{crowder} is the volume occupied by the major source of crowding, v_{other} the volume occupied by other macromolecules, and v_{water} the volume occupied by water in the cell. v is the volume of the cell. The maximum fraction of crowder in the cell is reached when the volume of water is close to 0, such that $\varphi_m \approx v_{\mathrm{crowder}} / (v_{\mathrm{crowder}} + v_{\mathrm{other}})$.

Validation of Doolittle equation and determination of parameters using instantaneous volume change through osmotic stress

During an instantaneous volume change as a result of an osmotic stress, the total number of macromolecules remains, to a first approximation, constant. The cell volume changes because of a passive outflow (hyper-osmotic stress) or inflow (hypo-osmotic stress) of water. We denote φ_0 the volume fraction of macromolecules before the osmotic shock, when the cell volume is v_0:

$$\varphi_0 = \frac{v_{\mathrm{crowder}}}{v_0} \tag{7}$$

Denoting $\tilde{v} = v / v_0$ the normalized cell volume, one can express Φ:

$$\Phi = \frac{\varphi}{\varphi_m - \varphi} = \frac{\varphi_0}{\varphi_m \tilde{v} - \varphi_0} \tag{8}$$

Note that the diffusion coefficient D_0 in equation 5 does not correspond to the coefficient of diffusion under normal conditions, but corresponds to the coefficient of diffusion for an infinitely diluted solution of macromolecules. Rather, the coefficient of diffusion under normal conditions, that we denote D_0', is defined when $\Phi = \Phi_0 = \frac{\varphi_0}{\varphi_m - \varphi_0}$

$$D'_0 = D_0 e^{-\zeta/\Phi_0} \tag{9}$$

which leads to the formula that describes the instantaneous change of the coefficient of diffusion upon a given volume change $\tilde{v}$:

$$\log\left(\frac{D}{D'_0}\right) = \zeta \frac{\varphi_0/\varphi_m}{1- \varphi_0/\varphi_m} \left(1 - \frac{1- \varphi_0/\varphi_m}{\tilde{v} - \varphi_0/\varphi_m}\right) \tag{10}$$

We used equation 10 to fit the coefficient of diffusion of 40nm-GEMs under hypo- and hyper-osmotic stresses (see figure 7A-B). The model is in good agreement with our data ($r^2 = 0.85$), and gives parameters for *S. cerevisiae* $\zeta = 0.6 \pm 0.2$, $\frac{\varphi_0}{\varphi_m} = 0.54 \pm 0.5$.

This number means that, under normal conditions, that the fraction of crowder inside the cell is about 50% the maximum crowding. This number is the non-osmotic volume, $\frac{\varphi_0}{\varphi_m} = v^*$, which corresponds to the volume of the cell occupied by macromolecules (Miermont et al., 2013).

We performed the same osmotic stress experiment on HEK293 cells, and initially measured different parameters ($\zeta \sim 1.6$, $\frac{\varphi_0}{\varphi_m} \sim 0.35$). Osmotic stress is known to strongly affect the actin cytoskeleton in mammalian cells, which could affect the interaction parameter, ζ, which was confirmed when we treated the cells with LatA at the same time we did the osmotic stress ($\zeta \sim 3.6$): the interaction parameter of the GEMs with the environment increased. When the actin cytoskeleton was stabilized with JLY cocktail, we found that the 2 parameters of the model were closer to the yeast values: ($\zeta \sim 0.6$, is very similar to yeast, suggesting that the interactions of the GEMs with the microenvironment is the same, and $\frac{\varphi_0}{\varphi_m} \sim 0.35$ is lower, suggesting that mammalian cells are less crowded.

This result suggest that 40nm-GEMs seem may interact with the same species inside both *S. cerevisiae* and HEK293 cells in a diffusion dependent manner.

Homeostatic crowding, and homeostasis breaking under a rapamycin treatment

What is the major source of crowding in the cell?

Our mutagenesis experiments suggested that mTORC1 controls cytosolic fluidity by tuning ribosome biogenesis and degradation. Therefore, ribosome concentration, and the concentration of proteins obtained through translation are candidates for the major source of crowding. We blocked translation using cycloheximide and found that the diffusion coefficient of 40nm-GEMs was not affected treatment (figure S2F-G). This result suggests that ribosomes are the most important source of crowding regulation for the 40nm-GEMs.

Therefore, we can re-write the volume fraction of crowder, considering ribosomes as the major crowder:

$$\varphi = \frac{v_{\text{ribo}}^{\text{total}}}{v} = \frac{c_{\text{ribo}}}{c^*} \tag{11}$$

with $c^* = 1 / v_{\text{ribo}}$, v_{ribo} being the typical volume of a single ribosome.

This leads to the following equation:

$$\log(D) = \zeta \frac{\varphi_0/\varphi_m}{1-\varphi_0/\varphi_m} \left(1 - \frac{1-c_{\text{ribo}}}{1-c_{\text{ribo}}\,\varphi_0/\varphi_m}\right) \tag{12}$$

We used this equation with the parameters measured by an osmotic stress to predict how particular mutations or chemical treatment should affect crowding, measured through the coefficient of diffusion, as a function of ribosome concentration. The ribosome concentration is determined by its number in the cells, N , and the volume of the cell, v . We measured the number of ribosomes N either by direct counting in EM, or their relative amount to wild-type or normal conditions was assessed by quantification of a total nucleic acid extraction run on an agarose gel (see Fig 7E-G). The cell volume was determined through brightfield measurements.

Fig. 6 displays the model prediction for both *S. cerevisiae* and HEK293 cells, which is in very good agreement with the measured data. This suggests that:

- Ribosomes are indeed the main determinant of cytosolic crowding inside the cell and can be considered as hard spheres.

- The cytoplasm of mammalian cells and yeasts behave similarly in terms of crowding.

Data and software availability

All subtomogram averages presented in this study have been deposited in the Electron Microscopy Data Bank (EMD-XXXX, EMD-XXXX, EMD-XXXX, EMD-XXXX), along with the tomograms from Figure 4 (EMD-XXXX, EMD-XXXX).

Supplementary movies

Supplementary movie 1

Bright field images (top panels), fluorescent images (middle panels) and fluorescent images with single particle trajectories superimposed (bottom panels), for DMSO (vehicle control, left) and rapamycin treated (right) *S. cerevisiae*. Related to figure 2D.

Scale bars are 5 μm. The movie playback speed is set to 100 frames per second (roughly real time), and the average time between frames is 8 ms. The time stamp shows seconds.

Supplementary movie 2

Fluorescent images (top panels) and fluorescent images with single particle trajectories superimposed (bottom panels), for DMSO (vehicle control, left) and rapamycin treated (right) HEK293 cells. Related to figure 2E. Scale bars are 4 μm. The movie playback speed is set to 100 frames per second (roughly real time), and the average time between frames is 8 ms. The time stamp shows seconds.

Supplementary movie 3

In situ cryo-ET of DMSO-treated control yeast cells. Related to figure 5A. The movie slices back and forth in Z through the tomographic volume, then reveals the 3D segmentation of the non-cytosolic volume (grey) and structures of the 40nm-GEMs (magenta), and then reveals the structures of the ribosomes (cyan).

Supplementary movie 4

In situ cryo-ET of rapamycin-treated yeast cells. Related to figure 5B. The movie slices back and forth in Z through the tomographic volume, then reveals the 3D segmentation of the non-cytosolic volume (grey; aggregates in dark grey) and structures of the 40nm-GEMs (magenta), and then reveals the structures of the ribosomes (cyan).

Supplementary tables

Table S2: Change in basal diffusion and in epistasis with rapamycin for various mutations. Related to figure 3.

Mutants in the BY4741 background expressing pLH0497. Basal change in diffusion coefficient, and epistatic effect with rapamycin were measured. Significant differences, defined when the basal change, or the epistasis effect are higher than 0.5, are highlighted in orange, as well as the corresponding gene. The two numbers presented are the change in basal gene diffusion, measured as the ratio of 40nm-GEM diffusion in the mutant as compared to the wild type:

$$Change\ in\ basal\ diffusion = \frac{D^{mut}}{D^{WT}}$$

and the epistatic effect with rapamycin, measured as the ratio change of the diffusion under rapamycin for the mutant *v.* the wild type (equation formulated such that 0 indicates no epistasis and 1 indicates complete epistasis):

$$magnitude\ of\ rapamycin\ effect = \varepsilon = 1 - \frac{\frac{D_{rapa}^{mut}}{D_{DMSO}^{mut}} - 1}{\frac{D_{rapa}^{WT}}{D_{DMSO}^{WT}} - 1}$$